

Dynamic Compression of Minerals in the MgO-
FeO-SiO₂ System

Thesis by

Joseph A. Akins

In Partial Fulfillment of the Requirements for the
degree of

Doctor of Philosophy

CALIFORNIA INSTITUTE OF TECHNOLOGY

Pasadena, California

2003

(Defended 30 May 2003)

© 2003

Joseph A. Akins

All Rights Reserved

Acknowledgements

This thesis would not have been possible without the guidance, friendship and assistance of numerous people. I'd like to thank my research adviser, Tom Ahrens, for his guidance and encouragement, and the rest of my committee: Dave Stevenson, George Rossman and Paul Asimow who was especially helpful in providing timely and insightful comments on the early drafts of this manuscript.

The "Experimental Geophysics Group" was also instrumental in completing the research included in this thesis. I thank Mike Long, Papo Gelle and Carl McCaughey for world class technical support in the lab. I can't thank Sue Yamada enough for always being so helpful. Shengnian Luo and Sarah Stewart-Mukhopadhyay provided immeasurable help in wading through the shock wave literature and greatly enhanced my growth as a scientist.

I'd also like to thank the Seismo Lab and Division staff for providing a virtually snag-free environment. I also thank all the other faculty, especially Jason Saleeby and Barclay Kamb, staff and graduate students too numerous to mention.

From outside the Caltech community, I'd like to thank my students at Glendale Community College for letting me pass on my excitement about Earth sciences; my best friend Veronika Aceves; and last, but not least, my family.

Dedication

This thesis is dedicated to the Sailors and Marines of Weapons Company, 2nd Battalion, 23rd Marine Regiment, 4th Marine Division, United States Marine Corps Reserve. They were called to active duty in January 2002 to serve their country and are presently attached to Task Force Tarawa, 1st Marine Expeditionary Force, to conduct combat missions in support of Operation Iraqi Freedom.

Abstract

The first shock wave experiments performed on silicate materials were reported for quartz in 1962. The intervening forty years have allowed for extensive investigation of SiO_2 by dynamic, static and theoretical means. Previous studies have concluded that quartz transforms completely to stishovite at ~ 40 GPa and melts at ~ 115 GPa along its Hugoniot. Recent discoveries that SiO_2 transforms to phases slightly more dense than stishovite have led to a reexamination of the dynamic compression of SiO_2 in this thesis. Based on comparing calculated Hugoniot data to data for multiple initial SiO_2 phases, it is proposed that, in addition to the stishovite and melt transitions, quartz is completely transformed to the CaCl_2 structure at ~ 70 GPa. Coesite shows evidence of complete transformation to stishovite at ~ 50 GPa, and to the CaCl_2 structure at ~ 65 GPa. Due to the higher temperature achieved in the quartz samples the slope of the stishovite- CaCl_2 phase boundary is constrained to be ~ 180 K/GPa.

From a similar analysis of Hugoniot data collected for high quality MgSiO_3 natural crystal and synthetic glass in this study, and existing data, it is concluded that along the crystal Hugoniot akimotoite is attained at ~ 70 GPa, perovskite structure at ~ 110 GPa and melt at ~ 170 GPa. It is found that the melt is 2-3 % denser than the solid at pressures greater than 100 GPa, after correcting for thermal differences in the two regimes. An important implication is a negative Clapeyron slope, leading to a decreasing melting temperature with increasing pressure, above ~ 100 GPa. These observations increase the possibility of the existence of a significant amount of partial melt in the lowermost mantle, e.g., the ultra low velocity zone.

Table of Contents

Acknowledgements	iii
Dedication	iv
Abstract	v
Table of Contents	vi
List of Tables	vii
List of Figures	viii
Chapter 1: Introduction.....	1
Outline of Thesis	1
Summary	1
Chapter 2: Hugoniot Equations of State Techniques and Calculations	3
Hugoniot Equations of State	3
Shock Temperature Measurements.....	5
Hugoniot Pressure-Temperature and Pressure-Density Calculations	6
Chapter 3: Dynamic Compression of SiO ₂ : A New Interpretation	21
Introduction.....	21
Dynamic Compression of Crystal Quartz.....	23
Hugoniot Sound Velocities in Quartz	24
Coesite, Porous Coesite and Porous Cristobalite Data	25
Shock Temperatures	27
Conclusions.....	31
Chapter 4: Shock Wave Equation of State and Temperature Measurements in (Mg,Fe)SiO ₃ Natural Crystal, Synthetic Glass and Porous Material.....	49
Introduction.....	49
Sample Preparation.....	49
Experimental Results.....	52
Dynamic Compression of Amorphous, Porous and Crystalline (Mg,Fe)SiO ₃ : Interpretation	52
Mixed Phase Regime.....	53
Calculated High Pressure Phase Hugoniots.....	55
Melting of MgSiO ₃ Perovskite: Constraints on Melting Curve at High Pressures	58
Conclusions.....	63
Bibliography	86

List of Tables

<i>Table</i>	<i>Page</i>
3.1 Elastic Parameter Values for SiO ₂ Phases	33
3.2 Thermodynamic Parameter Values for SiO ₂ Phases	34
4.1 MgSiO ₃ Glass and Crystal Electron Microprobe Analysis	65
4.2 Shock Wave Data for MgSiO ₃ Natural Crystal and Synthetic Glass .	66
4.3 Elastic Parameter Values for MgSiO ₃ and MgO Phases.....	67
4.4 Thermodynamic Parameter Values for MgSiO ₃ and MgO Phases.....	68
4.5 Wave Velocities for Various (Mg,Fe)SiO ₃ Phases	69
4.6 Constraints on Slope of MgSiO ₃ Melting Curve.....	70

List of Figures

<i>Number</i>	<i>Page</i>
2.1 Target Configurations.....	11
2.2 Diagrammatic Sketch of Impedance Match Method.....	13
2.3a Spectral Radiance vs. Time	15
2.3b Spectral Radiance vs. Wavelength.....	16
2.3c Emissivity vs. Time	17
2.3d Temperature vs. Time.....	18
2.4 Energy Balance.....	20
3.1 New Interpretation of Quartz Hugoniot Data	36
3.2a Hugoniot Sound Speed Measurements in Quartz	38
3.2a Hugoniot Sound Speed Measurements in Quartz: Interpretation ...	39
3.3 Hugoniot Data and Calculations for Coesite	41
3.4 Hugoniot Data and Calculations for Cristobalite and Fused Quartz.	43
3.5 Hugoniot Temperatures in Fused and Crystal Quartz.....	45
3.6a Shock Temperature Calculations for Solid Phases.....	47
3.6b Additional Studies of Stishovite-CaCl ₂ Phase Boundary	48
4.1 Interpretation of MgSiO ₃ Hugoniot Data.....	72
4.2 Calculated MgSiO ₃ Hugoniots in the 10 to 100 GPa Range.....	74
4.3 Calculated Shock Temperatures in the 10 to 100 GPa Range.....	76
4.4 Calculated MgSiO ₃ Hugoniots in the 100 to 200 GPa Range.....	78
4.5a Shallow Slope Extrapolation of MgSiO ₃ Melting Curve	80
4.5b Steep Slope Extrapolation of MgSiO ₃ Melting Curve.....	81
4.6 $\Delta V_m/V_s$ vs. Thermal Expansivity of Perovskite	83
4.7 (Mg,Fe)SiO ₃ Hugoniot Data.....	85

Chapter 1

Introduction

Outline of thesis

The body of this thesis consists of four chapters. Chapter 2 provides a brief explanation of the experimental techniques used, and a tutorial on calculating pressure-density and pressure-temperature Hugoniot. Chapter 3 is an attempt to reconcile pre-existing Hugoniot and static data in the SiO₂ system. The majority of Chapter 3 was previously published in *Geophysical Research Letters* [Akins and Ahrens, 2002]. The Hugoniot behavior observed in SiO₂ is used as a framework in analyzing the MgSiO₃ Hugoniot data collected in this study as presented in Chapter 4.

Summary

The discovery of the ultra-low-velocity zone (ULVZ) by *Garnero and Helmberger* [1995] and subsequent interpretation of the layer as being due to partial melt by *Williams and Garnero* [1996] has greatly increased the geophysical interest in silicate melts at pressures greater than 100 GPa. Although it is not known if SiO₂ exists as a free phase in the lower mantle, it has been extensively studied both statically and dynamically. The high pressure melt equation of state of SiO₂ is constrained by Hugoniot pressure-density, pressure-temperature and sound velocity data and provides a guide to predicting the behavior of silicate melts at high pressures. The occurrence of melting along the Hugoniot of fused and crystal quartz was first proposed by *Lyzenga et al.* [1983] based on shock temperature measurements and later verified by the sound velocity measurements of

Chhabildas and Miller [1985]. The fused quartz data exhibits a large amount of scatter; however, it is clear from the quartz data that with increasing pressure above 70 GPa the shock temperature rises steadily until at ~ 115 GPa a sudden drop in temperature of ~ 2000 K occurs. The temperature drop is assumed to be due to complete melting of the samples shocked to pressures greater than 115 GPa. A corresponding jump in density is observed and can be attributed to thermal expansion of the superheated solid relative to the melt regime of the Hugoniot. In spite of this super-heating, calculations of complete transformation to stishovite and CaCl_2 structure indicate that stishovite is attained along the Hugoniot of SiO_2 phases with a range of initial densities, from 2.13 to 2.92 g/cm^3 , and further transition to CaCl_2 structure for samples with initial densities of 2.65 to 2.92 g/cm^3 . The possibility that the CaCl_2 structure is attained along Hugoniot that reach the necessary pressure-temperature conditions is an unexpected result, however it is the favored interpretation of the data presented in Chapter 3.

The observations of super-heating, and an increase in density upon melting, in the SiO_2 Hugoniot data is considered in the analysis of the Hugoniot data on MgSiO_3 single crystal and glass presented in Chapter 4. Between 110 and 170 GPa the Hugoniot data for the crystal is in reasonable agreement with a calculated Hugoniot curve assuming the perovskite structure is achieved. At ~ 170 GPa there is a jump in density of $\sim 7\%$ observed in the data. Based on assumed behavior similar to that of quartz this jump is interpreted as being due to complete melting. Although there are numerous uncertainties involved, a thermal correction of the presumed perovskite state to the pressure and temperature of the melt indicates the melt is 2-3% denser than the solid. Implications of this observation are discussed further in Chapter 4.

Chapter 2

Hugoniot Equations of State Techniques and Calculations

Hugoniot Equations of State

Various techniques used to study the shock behavior of materials and the underlying math and physics are presented in a more complete form in *Ahrens* [1987] and are reviewed here only briefly. The equations governing a steady shock wave with velocity U_S relative to the laboratory, traveling through a sample with zero initial velocity and at room pressure, are

$$\rho_H = \frac{\rho_o U_S}{U_S - U_P}, \quad (\text{Conservation of mass}) \quad (2.1)$$

$$P_H = \rho_o U_S U_P \quad (\text{Conservation of momentum}) \quad (2.2)$$

and

$$\Delta E_H = E_H - E_o = \frac{1}{2} P_H (V_o - V_H) \quad (\text{Conservation of energy}) \quad (2.3)$$

where ρ , U_P , P and E refer to density, particle velocity behind the shock front, shock pressure, and internal energy. Subscript o refers to the unshocked state and subscript H refers to the peak shock state. In general there is a linear relation between U_S and U_P defined by the terms C_o and S in the form

$$U_S = C_o + S U_P, \quad (2.4)$$

and referred to as the Hugoniot equation of state. Standard materials, such as copper, aluminum and tantalum used in this study [Mitchell and Nellis, 1981] with well-constrained Hugoniot equations of state are used to constrain the equations of state of materials with unknown Hugoniot properties, such as the enstatite glass and crystal discussed in Chapter 4.

A projectile with a flyer plate of standard material embedded in it is launched at a target of the material being investigated (Figure 2.1a). The flyer plate impacts a driver plate at velocity U_{fp} and a shock is driven back into the flyer plate slowing it from U_{fp} to U_P along its Hugoniot (Figure 2.2) and forward into the driver plate, previously at rest. The sample being studied, with preshock density ρ_o , is in contact with the driver plate. As the shock passes from the driver into the sample the material is accelerated to particle velocity, U_{PH} . The shock travel time through the sample, U_S , is measured from a streak camera image. The streak camera records the reflection of a light source off of mirrored surfaces in contact with the sample and driver plate (Figure 2.1a). The arrival of the shock destroys the mirrored surface and the reflection of light being recorded is extinguished. Time calibration of the streak rate allows the shock travel time, and therefore velocity through the sample with known thickness, to be calculated.

From Equation 2.2 it is easily seen that there is a linear relation between particle velocity and pressure with slope $\rho_o U_S$ (Figure 2.2). Since the P- U_P curve of the standard material is known, the pressure-particle velocity state achieved in the sample is constrained by the intersection of the standard Hugoniot and the line with slope $\rho_o U_S$. Pressure is continuous across the driver-sample interface. The internal energy change upon reaching

the final shock state, ΔE_H , and the volume, V_H , of the shock state are then calculated from Equations 2.1 and 2.3.

Shock Temperature Measurements

Lyzenga [1980] reported the results of the first shock temperature measurements on Earth related materials. His thesis contains a more detailed explanation of the optical pyrometry method used to measure shock temperatures and a discussion of more recent upgrades to the Caltech system is found in Wenbo Yang's thesis [*Yang*, 1996]. A single shock temperature measurement was made in this study on MgSiO_3 glass, so only a brief introduction is provided here.

In contrast to the equation of state (EOS) experiments discussed previously shock temperature samples are not covered with a mirrored surface (Figure 2.1b). This allows light emitted from the shock front to be directed into a six channel optical pyrometer. To prepare the sample for shock temperature measurement a silver layer was sputter coated to the driver side of the sample to block radiation emitted from shock compressed air trapped in the sample-driver interface [*Lyzenga*, 1980]. To prevent the detection of light from non-planar shock waves, reflected from the sample edges, a mask with a 5 millimeter hole in the center was placed on the far side of the sample. Upon impact of a copper flyer plate with the target a shock wave was driven into a copper driver plate in contact with the sample. The sample pressure obtained by the shock impedance method discussed above, using the measured copper impactor speed of 5.97 ± 0.01 km/s and equation of state values for the glass of $C_0 = 4.29$ km/s and $S = 1.22$ determined from the three pressure-density Hugoniot experiments on MgSiO_3 glass listed in Table 4.2, was 107 ± 4 GPa. Radiation produced by the shock heating of the central 5 millimeters of the sample is reflected by a

disposable mirror into the optical system [Yang, 1996], which projects the image onto a fiber bundle. The fiber bundle is split into six smaller bundles that pass through 10 nm nominal band-pass interference filters centered at 451.3, 555.3, 603.7, 661.4, 748.3, and 904.0 nm. Digital oscilloscopes with 1 GHz sampling rate were used to record voltage versus time at each of the six wavelengths. The voltages are converted to light intensity by using a calibration factor obtained by measuring the voltages produced upon imaging a 1000 W spectral irradiance standard lamp (Optronix S-809) prior to each experiment. A sample trace from each channel used in the analysis of Shot 311 on MgSiO₃ glass is shown in Figure 2.3a. The light intensity, I , vs. wavelength, λ , at each sampling point is fit by a least-squares method to a greybody Planck radiation curve

$$I = \varepsilon C_1 \lambda^{-5} \left(e^{\frac{C_2}{\lambda T}} - 1 \right)^{-1} \quad (2.5)$$

where ε is effective emissivity, $C_1 = 1.191 \times 10^{-16}$ W m²/steradian and $C_2 = 1.439 \times 10^{-2}$ m K, shown in Figure 2.3b. This fit gives emissivity and temperature as a function of time during the experiment (Figure 2.3c and d). The scatter in these plots is due to the noise in channel 6 (Figure 2.3a). The inferred temperature in MgSiO₃ glass shocked to 107 GPa is 5050 ± 173 K with an emissivity of 0.78 ± 0.13 .

Hugoniot Pressure-Temperature and Pressure-Density Calculations

One way to calculate the Hugoniot temperature of a material shocked to a high pressure phase (H.P.P.), such as quartz shocked to stishovite, is to use energy balance to relate the Hugoniot state, P_H , at constant volume, V_H , to a metastable isentrope centered on

the fictive zero pressure volume, V_o , of the H.P.P. [Ahrens, 1987]. This statement is illustrated graphically in Figure 2.4. The energy balance is

$$\Delta E_H = E_{\text{TRAN}} + \Delta E_S + \Delta E_V \quad (2.6)$$

where ΔE_H , Hugoniot energy, is the change in internal energy due to shock compression of the material from V_{o0} to V_H (Equation 2.3); E_{TRAN} , transition energy, is the change in internal energy resulting from transformation of the low pressure phase (L.P.P.) to the H.P.P. at ambient conditions; ΔE_S is the energy change resulting from isentropic compression of the metastable H.P.P. from V_o to V_H ; and ΔE_V is the energy of heating the material at constant volume from the isentrope to the Hugoniot calculated using the definition of the thermodynamic Grüneisen parameter

$$\gamma = V \left(\frac{\partial P}{\partial E} \right)_V \approx \frac{V_H (P_H - P_S)}{E_H - E_S} \quad (\text{Mie-Grüneisen approximation}) \quad (2.7)$$

and the relation

$$\Delta E_V = E_H - E_S \quad (2.8)$$

which yields

$$\Delta E_V = \frac{V_H (P_H - P_S)}{\gamma} \quad (2.9)$$

Equation 2.6 may be rewritten

$$\frac{(V_{o0} - V_H)P_H}{2} = E_{\text{TRAN}} - \int_{V_o}^{V_H} P_S dV + \frac{(P_H - P_S)V_H}{\gamma} \quad (2.10)$$

Solving for P_H , an equation for calculating the Hugoniot of the initial sample shocked to the H.P.P., as a function of volume, is developed,

$$P_H = \frac{P_S + \frac{\gamma}{V_H} \left(\int_{V_0}^{V_H} P_S dV - E_{\text{TRAN}} \right)}{1 - \frac{\gamma}{V_H} \left(\frac{V_{00} - V_H}{2} \right)}. \quad (2.11)$$

Since the change in enthalpy, ΔH , during a phase transition and not the internal energy difference, E_{TRAN} , is measured by calorimetric studies, the following approximation is made,

$$E_{\text{TRAN}} = \Delta H + P\Delta V \approx \Delta H, \quad (2.12)$$

since $P\Delta V$ is negligible at 1bar. The Birch-Murnaghan EOS has shown great success in applications to shock wave data so it is used here,

$$E_S = 9 V_0 K_{oS} (f^2/2 + a_1 f^3/3) \quad (2.13)$$

$$P_S = 3 K_{oS} f (2f + 1)^{5/2} (1 + a_1 f), \quad (2.14)$$

where

$$f = [(V_0/V_H)^{2/3} - 1]/2 \quad (2.15)$$

$$a_1 = 3 (K_{oS}' - 4)/2 \quad (2.16)$$

K_{oS} and K_{oS}' are the bulk modulus of the H.P.P. at ambient conditions and its pressure derivative.

The equations describing Hugoniot temperatures by relating the H.P.P. Hugoniot to a metastable H.P.P. isentrope, or other reference curve, are

$$T_s = T_o \exp\left[-\int_{V_o}^{V_H} (\gamma/V)dV\right] \quad (2.17)$$

where

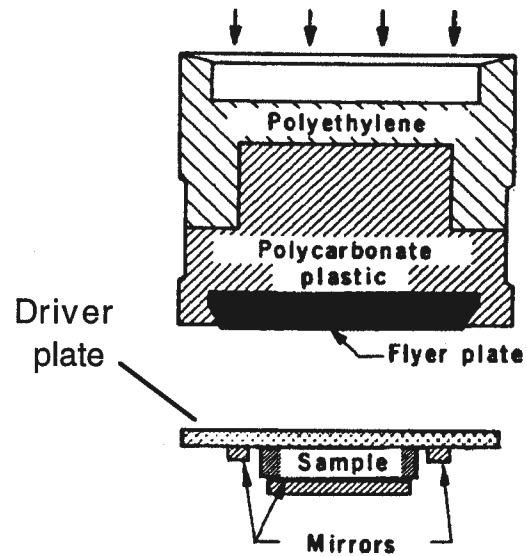
$$\gamma(V) = \gamma_o \left(\frac{V}{V_o}\right)^q \quad (2.18)$$

and

$$\int_{T_s}^{T_H} C_v dT = (P_H - P_s)V_H/\gamma. \quad (2.19)$$

Figure 2.1 Flyer plate impacts driver plate sending a plane shock wave into the sample. **a)** A xenon lamp, reflected by mirrors until the shock wave arrives, allows travel time through sample to be determined. After *Ahrens* [1980]. **b)** Silver coating on sample blocks gap flash from detectors. Radiation from shock front is detected. After *Schmitt et al.* [1986].

a) Equation of State target



b) Shock temperature target

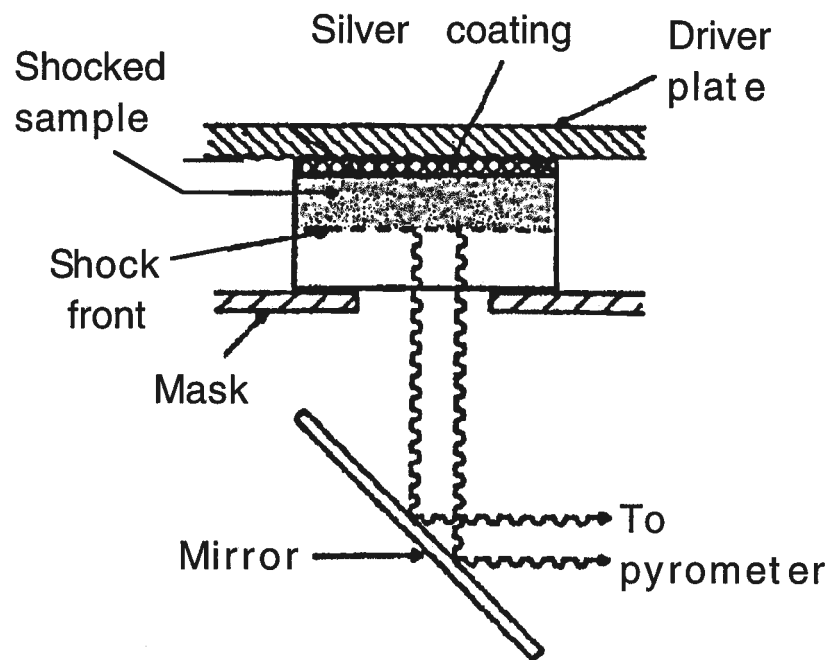


Figure 2.2 Digrammatic sketch of impedance match method for obtaining Hugoniot states discussed in text. After *Ahrens* [1987].

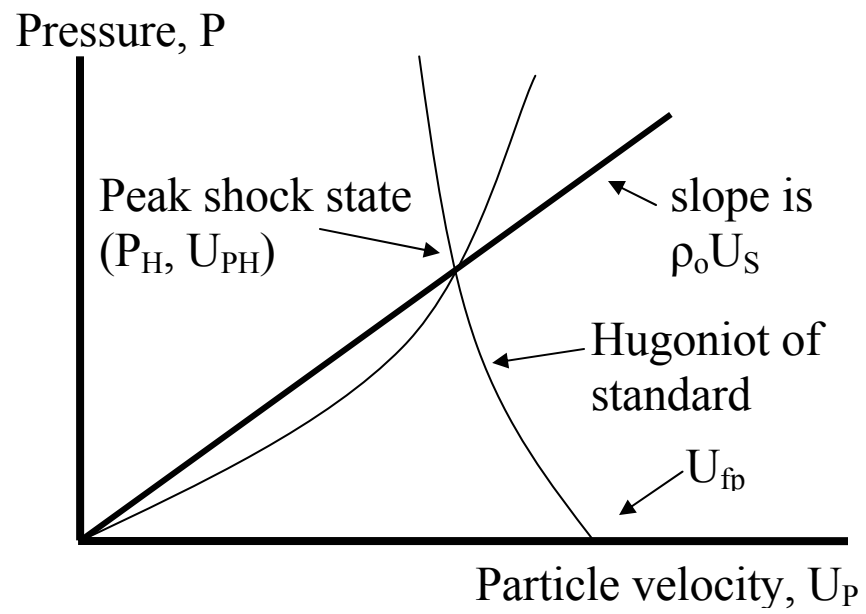
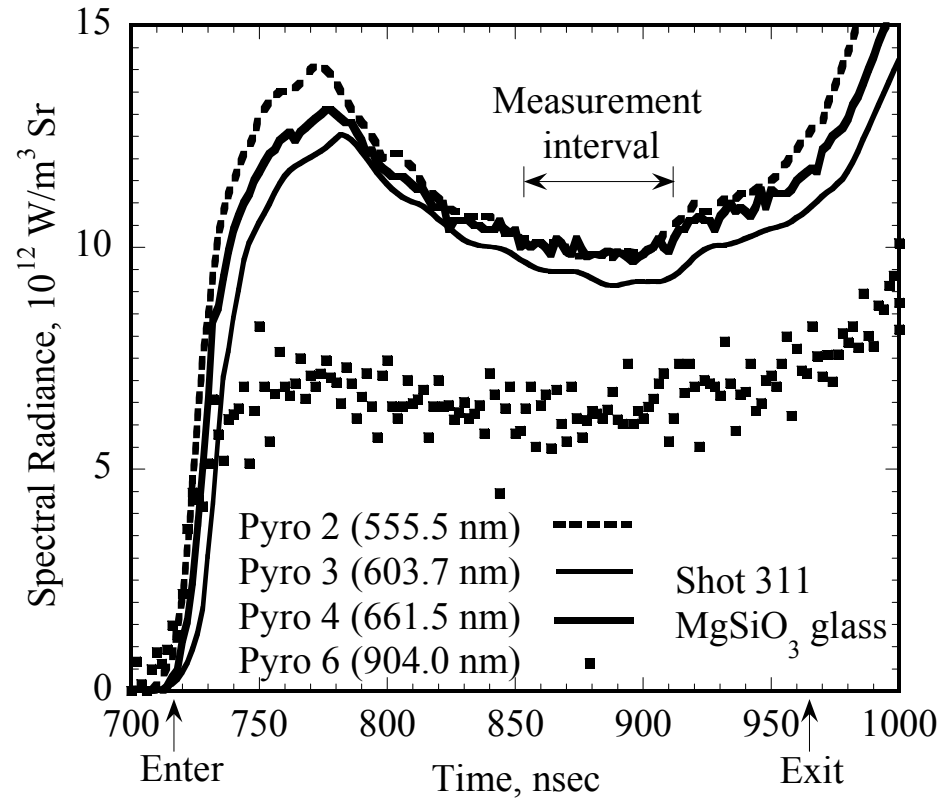
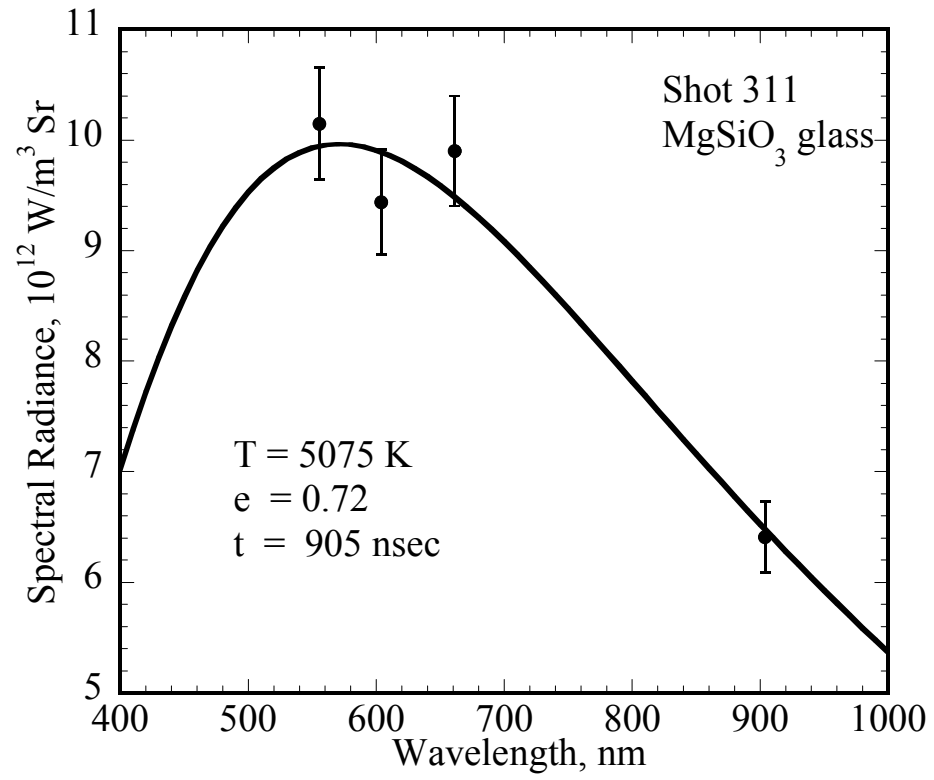
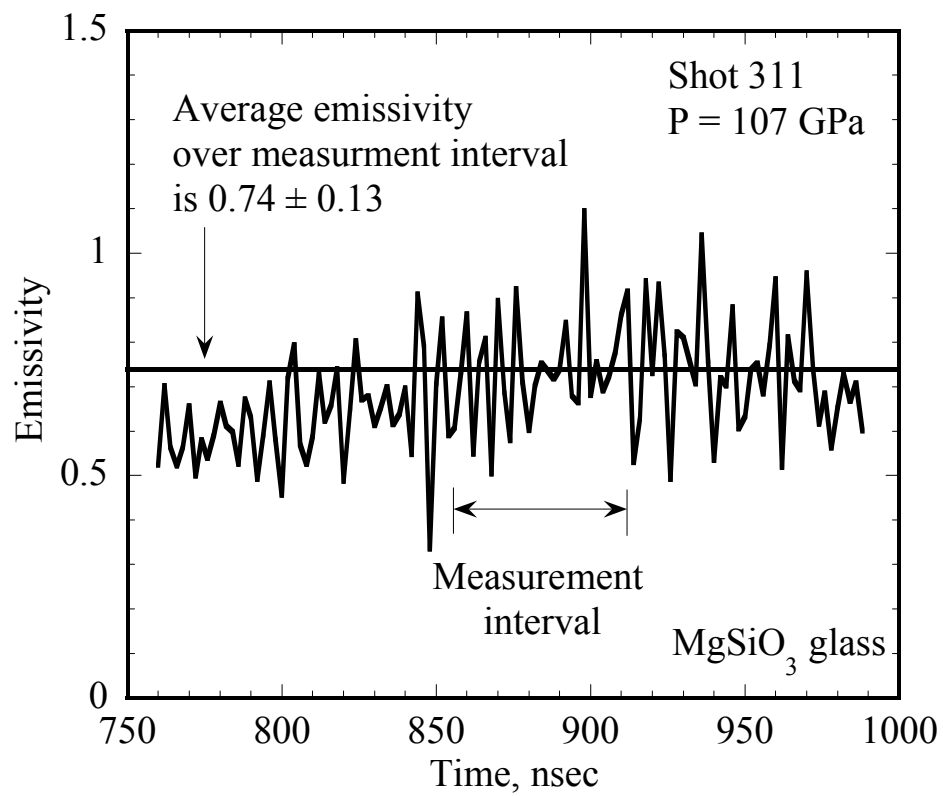


Figure 2.3 **a)** Spectral radiance vs. time obtained from voltage vs. time recorded by four pyrometer channels in shot 311. Pyrometers 1 and 5 were off scale and not presented. The initial peak in radiance is from "gap flash" as the shock passes from the driver into the sample. The trough is interpreted as the equilibrium state. The voltage measured was converted to radiance by calibrating to a standard lamp before the experiment. Estimated times of shock entrance and exit from sample are shown. **b)** A greybody temperature fit at a specific time is obtained by fitting radiance vs. wavelength points to a greybody Planck curve (Equation 2.5). 1σ standard errors for radiance at each wavelength are shown. **c)** Emissivity vs. time. Error is standard deviation (s.d.) of 29 data points in the measurement interval. Excessive variations are due to noise in one channel. **d)** Temperature vs. time. Error is s.d. of 29 data points in the measurement interval.







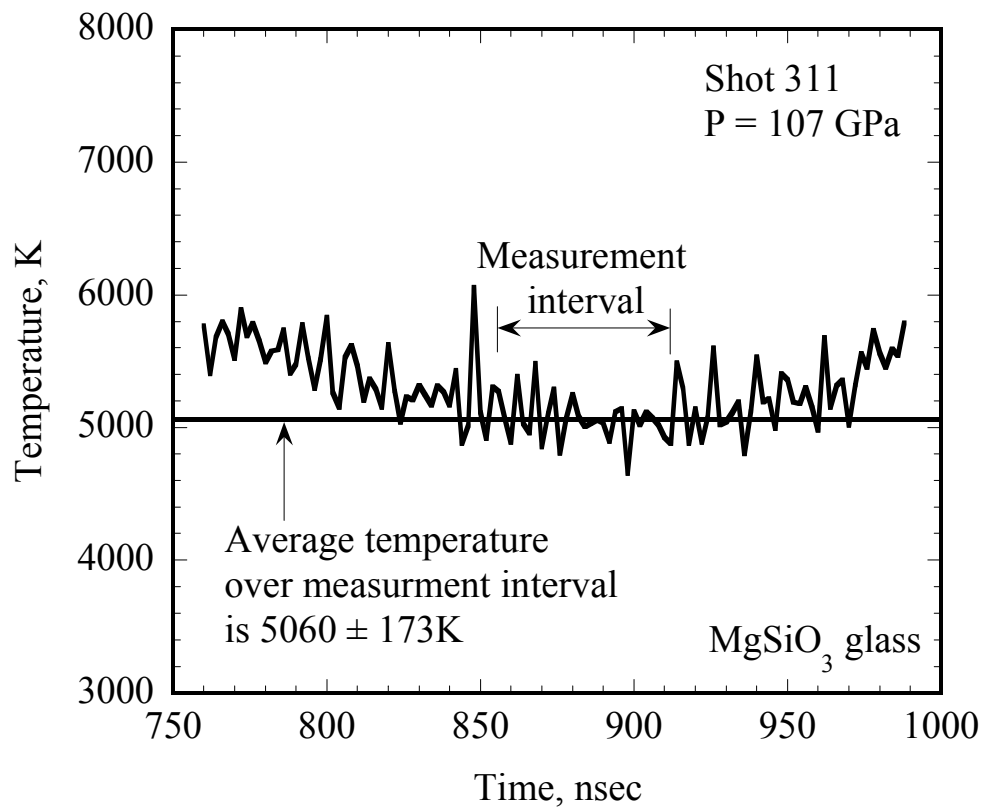
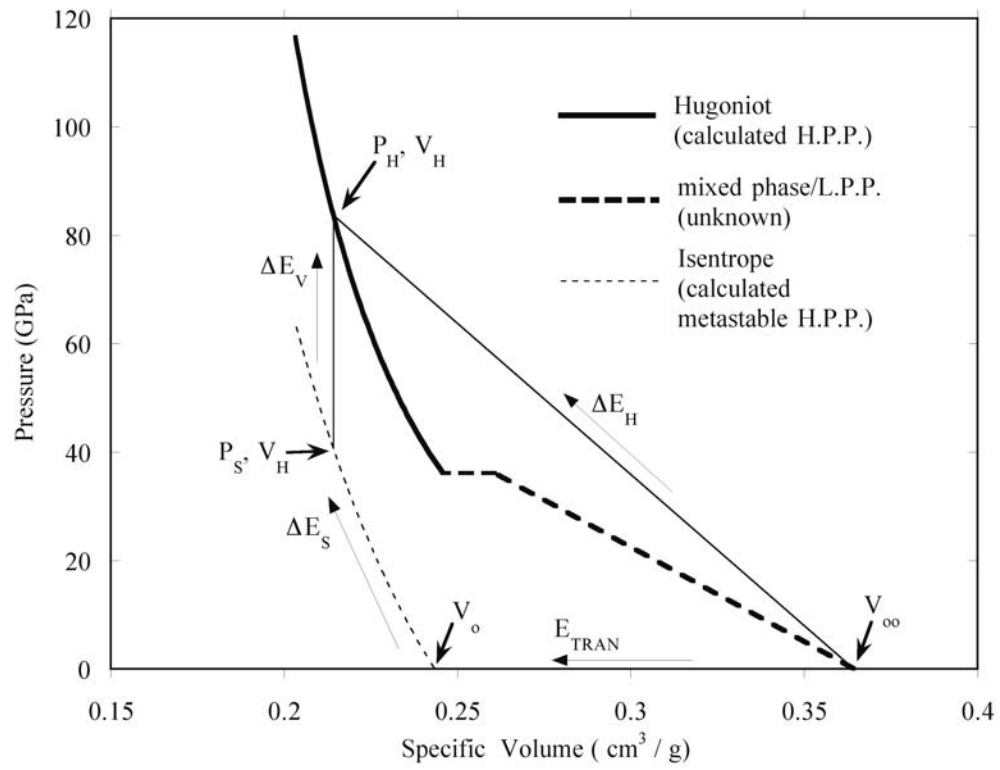


Figure 2.4 Equation 2.6 depicted graphically. ΔE_H , Hugoniot energy, is the change in internal energy due to shock compression of the material from V_{oo} to V_H (Equation 2.3); E_{TRAN} , transition energy, is the change in internal energy resulting from transformation of the low pressure phase (L.P.P.) to the H.P.P. at ambient conditions; ΔE_S is the energy change resulting from isentropic compression of the metastable H.P.P. from V_o to V_H ; and ΔE_V is the energy of heating the material at constant volume from the isentrope to the Hugoniot.



Chapter 3

Dynamic Compression of SiO₂: A New Interpretation

Introduction

The recent discoveries of silica phases with the CaCl₂ ($\rho_0 = 4.303 \text{ g/cm}^3$) [Andrault *et al.*, 2003] and α -PbO₂ ($\rho_0 = 4.334 \text{ g/cm}^3$) [Teter *et al.*, 1998] structures, slightly more dense than stishovite ($\rho_0 = 4.287 \text{ g/cm}^3$) [Weidner *et al.*, 1982], have led to a reexamination of the dynamic compression of SiO₂. Although the first observation of the CaCl₂ structure indicated it was stable above $\sim 100 \text{ GPa}$ [Tsuchida and Yagi, 1989], later theoretical [Cohen, 1991] and experimental [Andrault *et al.*, 2003; Dubrovinsky *et al.*, 1997; Kingma *et al.*, 1995; Shieh *et al.*, 2002] studies have constrained the onset of the stishovite-to-CaCl₂ transition to $\sim 50 \text{ GPa}$ at 298K. The α -PbO₂ structure is found to be stable above $\sim 100 \text{ GPa}$, based on experiments and theoretical calculations [Dubrovinskaia *et al.*, 2001; Dubrovinsky *et al.*, 2001; Dubrovinsky *et al.*, 1997; Murakami *et al.*, 2003; Teter *et al.*, 1998]. The α -PbO₂ structure has also been observed in the Shergotty meteorite, a Martian basalt thought to have experienced multiple shock events [El Goresy *et al.*, 2000]. In addition to these high-pressure silica phases, with oxygen in 6-fold coordination, transition to an 8-fold coordination structure is predicted near 200 GPa [Dubrovinsky *et al.*, 1997; Teter *et al.*, 1998]. Although it is unclear whether substantial quantities of a phase of SiO₂ exists in the Earth's mantle, the equations of state of high-pressure SiO₂ phases play a crucial role in mantle-core chemical reactions which sequester iron from mantle silicates into the core [Luo *et al.*, 2002b].

In addition to the static data on SiO₂ there have been several studies on its dynamic compression. Crystal and fused quartz were the first silicates studied by dynamic compression methods [Adadurov *et al.*, 1962; Wackerle, 1962]. Thereafter McQueen *et al.* [1963] demonstrated that the Hugoniot of crystal ($\rho_0 = 2.65 \text{ g/cm}^3$) and fused ($\rho_0 = 2.2 \text{ g/cm}^3$) quartz, above 40 GPa, correspond to the properties of the rutile structure of SiO₂ [Stishov and Popova, 1961], which was later found in shocked quartz-bearing rocks of Meteor Crater [Chao *et al.*, 1962] and named stishovite. Subsequently, small amounts of stishovite were recovered from peak pressures in the 15-28 GPa range [DeCarli and Milton, 1965]. Later work by German *et al.* [1974] demonstrated that orthorhombic SiO₂ may be recovered from the 70-90 GPa (first shock) pressure range along the Hugoniot of quartz. This phase ($\rho_0 = 4.435 \text{ g/cm}^3$) was most likely formed during release from a multiply shocked state and is not necessarily representative of a phase formed along the principal Hugoniot of quartz.

Additional studies of crystal and fused quartz, as well as porous cristobalite ($\rho_0 = 2.13 \text{ g/cm}^3$), porous coesite ($\rho_0 = 2.4 \text{ g/cm}^3$), coesite ($\rho_0 = 2.92 \text{ g/cm}^3$), and stishovite ($\rho_0 = 4.3 \text{ g/cm}^3$) have been conducted by Fowles [1967], Trunin *et al.* [1971], Podurets *et al.* [1990], Borshchevskii *et al.* [1998], Lyzenga *et al.* [1983], Zhugin *et al.* [1999] and Luo *et al.* [2002b]. It is proposed in this work that with the exception of the more scattered fused quartz results, and two anomalous points for porous cristobalite, these data provide strong evidence for the transitions to stishovite, the CaCl₂ structure and melt along the Hugoniots of quartz and coesite, whereas porous coesite melts directly from the stishovite regime. Shocked stishovite does not appear to undergo any phase changes up to 240 GPa [Luo *et al.*, 2002b].

Dynamic Compression of Crystal Quartz

The present interpretation of the crystal quartz Hugoniot is shown in Figure 3.1. The theoretical Hugoniot pressure-density and pressure-temperature calculation for crystal quartz (and other SiO₂ phases) of Figures 3.1, 3.3 and 3.4 are based on the Mie-Grüneisen offset from the 3rd order Birch-Murnaghan isentropes, e.g., *McQueen et al.* [1963], as outlined in Chapter 2. Based on the phase diagram of Figure 3.6a and the independent pressure-density and pressure-temperature Hugoniot data for various silica phases, the following seven regimes along the quartz Hugoniot are inferred: 1) The elastic shock Hugoniot extending to 5.5 – 15.0 GPa depending on orientation [*Fowles, 1967; Wackerle, 1962*]. 2) Mixed phase regime (A) of quartz and stishovite extending from 23 to 35 GPa [*Zhugin et al., 1999*]. 3) The stishovite regime from 35 to 70 GPa, which is consistent with the equation of state (EOS) parameters for stishovite in Tables 3.1 and 3.2. 4) Mixed phase regime (B) of stishovite and CaCl₂ (~70 GPa). 5) The CaCl₂ structure regime from 70 to 115 GPa. The Hugoniot in this regime is consistent with parameters for CaCl₂ structure given in Tables 3.1 and 3.2. 6) Mixed phase regime (C) of CaCl₂ and melt. 7) The high pressure phase (H.P.P.) melt regime > 120 GPa. The Hugoniot from 120-400 GPa is consistent with the H.P.P. melt EOS parameters in Tables 3.1 and 3.2 and is assumed to be dominated by silicon in 6-fold coordination. The jump in density observed upon achieving final shock states in the melt is discussed in detail by *Lyzenga et al.* [1983] and briefly in this work in relation to the corresponding shock temperature measurements.

The room temperature compression curves of stishovite and the CaCl₂ structure, observed in the diamond anvil study of *Andraut et al.* [2003], are plotted below the shock wave data in Figure 3.1. Notably the diamond anvil data displays a transition at ~ 50 GPa

from stishovite to the CaCl_2 structure in approximate agreement with the deviation of the calculated 298K isotherms of stishovite and the CaCl_2 structure. The EOS for stishovite used in the present study is further supported by the reasonable agreement of the calculated stishovite Hugoniot and the data of *Luo et al.* [2002b] in the 100 to 240 GPa range (inset Figure 3.1).

The interpretation of the quartz Hugoniot presented in this study, based largely on the EOS of stishovite, is in stark contrast to the conclusion of *Panero et al.* [2003] that the Hugoniot data is 2.4% less dense than calculated for complete conversion of quartz to stishovite, even though the same EOS parameters were used. Due to this discrepancy the calculation of quartz shocked to stishovite was independently verified by Professors Thomas J. Ahrens and Paul D. Asimow, and Dr. Shengnian Luo, all at Caltech, and found to be in perfect agreement with the calculation presented in Figure 3.1 [personal communications].

Hugoniot Sound Velocities in Quartz

The measurements of sound velocity behind the shock front in dynamically compressed crystal quartz ($\rho_0 = 2.65 \text{ g/cm}^3$), quartzite ($\rho_0 = 2.65 \text{ g/cm}^3$) and novaculite ($\rho_0 = 2.64 \text{ g/cm}^3$) shown in Figure 3.2, support the above interpretation of the high pressure behavior of quartz along the Hugoniot. Figure 3.2a shows calculated longitudinal and bulk sound velocities, after *Duffy and Ahrens* [1992] for stishovite, CaCl_2 structure and H.P.P. melt. Elastic parameter values used are listed in Table 3.1. The values of K_0 , K' , and ρ_0 for the H.P.P. melt were varied to satisfy the sound velocity data, and the pressure-density (Figure 3.1) and pressure-temperature (Figure 3.5) Hugoniot data discussed later. The interpretation of the sound velocities is presented in Figure 3.2b. The rarefaction velocities

for elastic and deformational unloading demonstrate that the stishovite longitudinal wave velocity increases to about 12.9 km/s, at 35 GPa, at which pressure mode softening (decreasing shear modulus) begins to occur [Cohen, 1991]. The mode softening results in an essentially second order phase transition from tetragonal stishovite to a similar orthorhombic CaCl_2 structure [Andraut *et al.*, 2003], as opposed to a first order reconstructive transition. With increasing pressure the sound velocity decreases in anticipation of the transition to the CaCl_2 structure which occurs at ~ 65 GPa. The longitudinal wave velocity in the CaCl_2 structure (metastably shocked into the melt region above 70 GPa) then rises again until at a Hugoniot pressure of 115 GPa melting occurs, as inferred by the sudden drop to the bulk sound velocity. At this pressure the longitudinal velocity becomes equal to the bulk velocity, as is expected upon melting. Although the dip in sound velocity indicated by the data may be due to random error, the agreement with expected behavior, given shear softening in stishovite prior to transformation to the CaCl_2 structure, is remarkable. In contrast to the longitudinal velocity, the bulk sound velocity should steadily increase at the onset of the stishovite to CaCl_2 structure transition and continue to increase with pressure. Quite interestingly, the bulk sound velocity data appear to change little upon melting of CaCl_2 structure at ~ 115 GPa.

Coesite, Porous Coesite and Porous Cristobalite Data

Shock data for coesite ($\rho_0 = 2.92 \text{ g/cm}^3$) and porous coesite ($\rho_0 = 2.4 \text{ g/cm}^3$) are plotted in Figure 3.3. The theoretical Hugoniot curves are consistent with the stishovite, CaCl_2 and melt EOS parameters of Tables 3.1 and 3.2. Coesite and porous coesite are assessed to transform to stishovite above 30 GPa. The single data for porous coesite at 85 GPa is assumed to correspond to a point in the stishovite-melt regime which achieves a

higher density than stishovite. In contrast the zero porosity polycrystalline coesite achieves a state in the 50 to 65 GPa region consistent with coesite transformed to stishovite, whereas the five higher pressure states between 85 and 140 GPa appear to lie along the CaCl_2 regime of the coesite Hugoniot; melt is inferred above 150 GPa as will be discussed in relation to the corresponding shock temperature calculations.

Hugoniot data for fused quartz and porous cristobalite compared to calculations for final shock states of stishovite, CaCl_2 structure, and H.P.P. melt are shown in Figure 3.4. In the case of the porous cristobalite data the two points in the 45 to 70 GPa region are interpreted as being in the stishovite regime. The calculations for porous cristobalite (thick lines) indicate the data greater than 70 GPa are too dense to be in the CaCl_2 structure, and not dense enough to be H.P.P. melt and are considered anomalous. Although they are referred to as α -cristobalite by *Podurets et al.* [1981] the quality of these samples is unknown. The reported average initial density of 2.13 g/cm^3 is less than the typical values for cristobalite of 2.2 to 2.33 g/cm^3 [*Gaines et al.*, 1997] and initial densities for each experiment are not tabulated. A possible explanation for the discrepancy with the calculated Hugoniots in this pressure regime will be discussed in tandem with observed anomalous behavior of the fused quartz Hugoniot data in the section on shock temperature calculations, below.

Regarding the fused quartz data, the majority of the data is bounded by the calculated stishovite and H.P.P. melt segments indicating complete conversion to stishovite, or melt, in contrast to the conclusion of *Panero et al.* [2003]. The scatter is most likely due to differing glass synthesis conditions, residual stress, or impurities in the samples. Related details are not provided in the shock wave studies tabulated by *Marsh*

[1980]. Although a more detailed study of the Hugoniot states achieved by fused quartz with uniform constraints on synthesis conditions and composition may prove useful, a similar region of Hugoniot P-V-T space may be explored using cristobalite, or possibly tridymite which typically has fewer impurities and can be found as centimeter sized crystals in lithophysal cavities of some rhyolitic rocks [*Gaines et al.*, 1997].

Shock Temperatures

Complete shock temperature data for both fused and crystal quartz, as well as calculations in the solid and melt phases, are shown in Figure 3.5, and for the solid Hugoniot states only, in Figure 3.6a. Shock temperatures were calculated using the method of *Ahrens et al.* [1982] as presented in Chapter 2 and assumed C_V equal to a constant for the solid phases (Tables 3.1 and 3.2). A temperature dependent C_V is required for the melt to satisfy the shock temperature measurements in the melt regime of fused and crystal quartz and calculations assuming both C_V constant and $C_V(T)$ are plotted in Figure 3.5. The temperature dependence used is similar to that of *Grover* [1971],

$$C_V = 3R[1 + 0.06(T/T_m)^2]. \quad (3.1)$$

The calculated shock temperatures of *Wackerle* [1962] for both fused and crystal quartz are in remarkable agreement with the original data of *Lyzenga et al.* [1983], as modified by *Boslough* [1988], and the *McQueen and Fritz* [1982] data. The agreement between the calculated Hugoniot and the data show the fused quartz shock temperatures below 55 GPa to be in the stishovite stability field, the data between 55 and 65 GPa appear to correspond to superheated stishovite, and above 75 GPa lie along the melt segment of the Hugoniot.

It now appears that in the case of crystal quartz the Hugoniot between 70 and 115 GPa is in the CaCl_2 structure rather than the superheated stishovite phase as suggested by *Lyzenga et al.* [1983]. Shock temperature states above 115 GPa are completely melted. The interpretation of super-heated solid followed by a drop in temperature due to melting is also supported by the post-shock temperature analysis of *Boslough* [1988]. Therefore the drop in shock temperature at 65-70 GPa for fused quartz corresponds to melting of stishovite, whereas the drop between 115 and 120 GPa for shocked crystal quartz results from melting of crystal quartz transformed to the CaCl_2 structure.

Notably, the shock temperature calculations (Figure 3.6a) for porous cristobalite indicate that it enters the regime of transition to stishovite above 20 GPa and the molten SiO_2 stability field at 70 GPa. Taken with the pressure-density Hugoniot data of Figure 3.4a, Figure 3.6a clearly demonstrates that, like fused quartz transformed to stishovite, porous cristobalite also is superheated along the stishovite branch of its Hugoniot to a shock pressure of 70 GPa. Therefore it is predicted that future shock temperature experiments will see a drastic decline in shock temperature from ~ 6200 to $\sim 4200\text{K}$ at ~ 70 GPa upon making radiative measurements in single crystal cristobalite, or tridymite as suggested previously. In light of the anomalous behavior of the fused quartz and porous cristobalite data these experiments would be very useful in constraining the assertions of this work that complete transition to high pressure phases occurs predictably in SiO_2 phases. It is proposed that the fused quartz and porous cristobalite data are sampling a P-V-T region in the melt where some portion of the silicon is still in 4-fold coordination, unlike the quartz H.P.P. melt segment that lies in melt that has completely undergone transition to 6-fold coordination.

Similarly, as shown in Figure 3.3, porous coesite appears to begin to transform to the stishovite structure above 30 GPa and is completely transformed into the stishovite regime at 55 GPa. Between 55 and 80 GPa it appears to remain in the stishovite structure although above 55 GPa the stishovite is superheated. The pressure-density data (Figure 3.3) suggest that melting of the superheated stishovite occurs at ~85 GPa and above ~90 GPa the Hugoniot is inferred to be in the complete H.P.P. melt regime in agreement with a similar amount of super heating to that observed in the quartz data, as shown in Figure 3.6a.

Coesite also demonstrates the phase transition to stishovite starting at 30 GPa, is in the coesite-stishovite mixed phase regime from 30 to 50 GPa and in the pure stishovite region from 50 to ~62 GPa. Transition from stishovite to the CaCl_2 structure appears to occur at ~65 GPa and, accounting for an amount of super-heating similar to that of quartz shocked to CaCl_2 , it is inferred that at ~150 GPa transition to the H.P.P. melt occurs. Given this new interpretation of the transformation from stishovite to the CaCl_2 structure along the quartz and coesite Hugoniots, at 70 and 65 GPa, respectively, the Clapeyron slope of the transition is constrained to be ~180 K/GPa. Other experimental and calculated constraints on the slope of the phase boundary are shown in Figure 3.6b. Due to the second order nature of the stishovite to CaCl_2 structure it is not surprising that the transition appears to occur near equilibrium conditions as predicted in two other studies [*Kingma et al.*, 1995; *Oganov et al.*, 2003]. This would most likely not be the case if the transition were reconstructive, e.g., first order.

Given the phase diagram of Figure 3.6a and the stishovite Hugoniot temperature calculation, stishovite is too cold to undergo any of the above mentioned solid-solid phase

transitions along its Hugoniot, as demonstrated by the stishovite Hugoniot data up to 240 GPa of *Luo et al.* [2002b], plotted along with the calculated Hugoniot in Figure 3.1. Not until 425 GPa will stishovite melt along its principal Hugoniot. To observe the solid-solid transitions shock wave experiments on porous stishovite, stishovite/coesite, or stishovite/paraffin mixtures are needed. The following predictions are made: For $\rho_0 = 3.6 \text{ g/cm}^3$ the CaCl_2 to $\alpha\text{-PbO}_2$ transition will be observed at $\sim 130 \text{ GPa}$ and $\sim 3000 \text{ K}$, and melting at $\sim 200 \text{ GPa}$ and $\sim 5000 \text{ K}$. For $\rho_0 = 3.95 \text{ g/cm}^3$ the CaCl_2 to $\alpha\text{-PbO}_2$ will be observed at $\sim 110 \text{ GPa}$ and $\sim 1700 \text{ K}$, $\alpha\text{-PbO}_2$ to 8-fold coordination solid at $\sim 200 \text{ GPa}$ and $\sim 3500 \text{ K}$, and melting at $\sim 315 \text{ GPa}$ and $\sim 5500 \text{ K}$.

The shock temperature (Figure 3.5) and sound velocity (Figure 3.2b) Hugoniot data indicate melting occurs at $\sim 115 \text{ GPa}$ along the quartz Hugoniot. Interestingly, at this pressure the Hugoniot melt regime lies at 2% higher density than the solid phase (Figure 3.1). Is the melt intrinsically denser than the solid in this pressure regime, or is the superheated solid segment of the quartz Hugoniot less dense due to being 2000 K hotter than the melt (Figure 3.5)? Given that the solid is superheated to $\sim 7000 \text{ K}$ before dropping in temperature 2000 K upon melting (Figure 3.5), a correction for this temperature difference is needed to place a constraint on the thermal contribution to the 2% density difference. The thermal expansion, α , of stishovite at 120 GPa and 4000 K was calculated to be $1.2 \times 10^{-5} \text{ K}^{-1}$ by *Luo et al.* [2002a]. Assuming CaCl_2 structure SiO_2 , the super heated solid phase along the quartz Hugoniot, has similar thermal properties to that of stishovite, $\alpha = 1.2 \times 10^{-5} \text{ K}^{-1}$ may be used to correct the density of the solid, 5.01 g/cm^3 , at 115 GPa for the 2000 K temperature difference between the super heated solid and melt to 5.13 g/cm^3 . This is close to the density of the melt, 5.15 g/cm^3 , at 115 GPa and 5000 K.

Given $\sim 2\%$ uncertainties in the Hugoniot density measurements inferred from shock travel times through samples during shock temperature experiments [Lyzenga *et al.*, 1983], the 2.7% density decrease inferred along the melt boundary by Lyzenga *et al.* [1983] and the 11 K/GPa positive Clapeyron slope (Equation 4.1) are compatible with the observed jump in density upon melting at 115 GPa.

Conclusions

Based on the preceding analysis the following conclusions are drawn:

- 1) The shock wave pressure-density data for porous cristobalite, fused quartz and porous coesite are consistent with these phases transforming from their initial state to the stishovite structure upon shock compression.
- 2) Based on shock temperature measurements in fused and crystal quartz, it is inferred that in porous cristobalite, fused quartz and porous coesite the solid is super-heated in the stishovite structure starting at 45, 55 and 60 GPa, respectively followed by melting at ~ 70 GPa for porous cristobalite and fused quartz and at ~ 85 GPa for porous coesite.
- 3) In contrast, shock induced transformation to stishovite from initially crystal quartz and coesite begins at 22 and 30 GPa, respectively. Complete transformation to stishovite is completed at 40-50 GPa along their Hugoniots and transformation to the CaCl_2 structure begins at 65 – 75 GPa. The CaCl_2 phase for crystal quartz and coesite is metastably superheated above the 80 GPa, 4000 K melting line of the CaCl_2 structure. Catastrophic melting occurs at ~ 115 GPa along the quartz

Hugoniot, and ~ 150 GPa along the coesite Hugoniot, in the CaCl_2 structure. At higher pressures the Hugoniots of crystal quartz and coesite lie in the melt regime.

- 4) Stishovite is too cold along its principal Hugoniot to undergo phase transitions up to 240 GPa. To observe the solid-solid transitions shock wave experiments on porous stishovite, stishovite/coesite, or stishovite/paraffin mixtures are needed. The following predictions are made: For $\rho_0 = 3.6 \text{ g/cm}^3$ the CaCl_2 to $\alpha\text{-PbO}_2$ transition will be observed at ~ 130 GPa and ~ 3000 K, and melting at ~ 200 GPa and ~ 5000 K. For $\rho_0 = 3.95 \text{ g/cm}^3$ the CaCl_2 to $\alpha\text{-PbO}_2$ will be observed at ~ 110 GPa and ~ 1700 K, $\alpha\text{-PbO}_2$ to 8-fold coordination solid at ~ 200 GPa and ~ 3500 K, and melting at ~ 315 GPa and ~ 5500 K.
- 5) Hugoniot sound velocity data for quartz provides evidence of shear softening in stishovite prior to transformation to the CaCl_2 structure at ~ 70 GPa.
- 6) The positive slope of 11 K/GPa inferred by *Lyzenga et al.* [1983] is consistent with the density jump associated with melting along the quartz Hugoniot at 115 GPa.

Table 3.1: Elastic Parameters of SiO₂ Phases

Phase	Initial Density, ρ_0 (g/cm ³)	Bulk Modulus, K_0 (GPa)	dK_0/dP , K'	Shear Modulus, G_0 (GPa)	dG_0/dP , G'
<u>SiO₂ Composition</u>					
Stishovite	4.287 ^{a)}	315 ^{b)}	4.8 ^{b)}	223 ^{c)}	1.72 ^{c)}
CaCl ₂ structure	4.303 ^{d)}	334 ^{d)}	4.0 ^{d)}	200 ^{e)}	1.6 ^{e)}
H.P.P. melt	4.100 ^{f)}	240 ^{f)}	6.0 ^{f)}	-	-

a) *Weidner et al.* [1982].

b) *Panero et al.* [2003].

c) *Karki et al.* [2001].

d) *Andrault et al.* [2003].

e) *Karki et al.* [1997].

f) This study (see text).

Table 3.2: Thermodynamic Parameters of SiO₂ Phases

Phase	Grüneisen Parameter, $\gamma_0^a)$	$q^a)$	Transition Energy, $E_{tr}^b)$ (MJ/kg)	Specific Heat, $C_v^c)$, (J/kg K)
<u>SiO₂ Composition</u>			<u>From quartz</u>	
Stishovite	1.35 ^{d)}	1.0 ^{e)}	0.86 ^{f)}	0.9*3nR ^{e)}
CaCl ₂ structure	1.2 ^{g)}	1.0 ^{g)}	1.3 ^{g)}	1.05*3nR ^{g)}
H.P.P. melt	0.5 ^{g)}	2.0 ^{g)}	2.5 ^{g)}	1.1*3nR ^{g), h)}

a) $\gamma = \gamma_0 (V/V_0)^q$

b) $E_{tr} = \Delta E \cong \Delta H$ at zero pressure.

c) $n = \#$ of atoms per formula unit.

d) *Stixrude and Bukowinski* [1993].

e) *Akins and Ahrens* [2002].

f) *Navrotsky* [1995].

g) This study.

h) $C_v(T)$ also used. See text.

Figure 3.1 New interpretation of Hugoniot of crystal SiO₂ (quartz). Quartz data (open circles) from *Marsh* [1980], *Fowles* [1967], *Trunin et al.* [1971], *Lyzenga et al.* [1983], *Podurets et al.* [1976], *Podurets et al.* [1990], *Borschevskii et al.* [1998]; Stishovite data (closed circles) *Luo et al.* [2002b]. Static compression data for initial stishovite (x's) from *Andrault et al.* [2003]. Curves in stishovite, CaCl₂ structure and H.P.P. melt regime calculated from parameters in Tables 3.1 and 3.2.

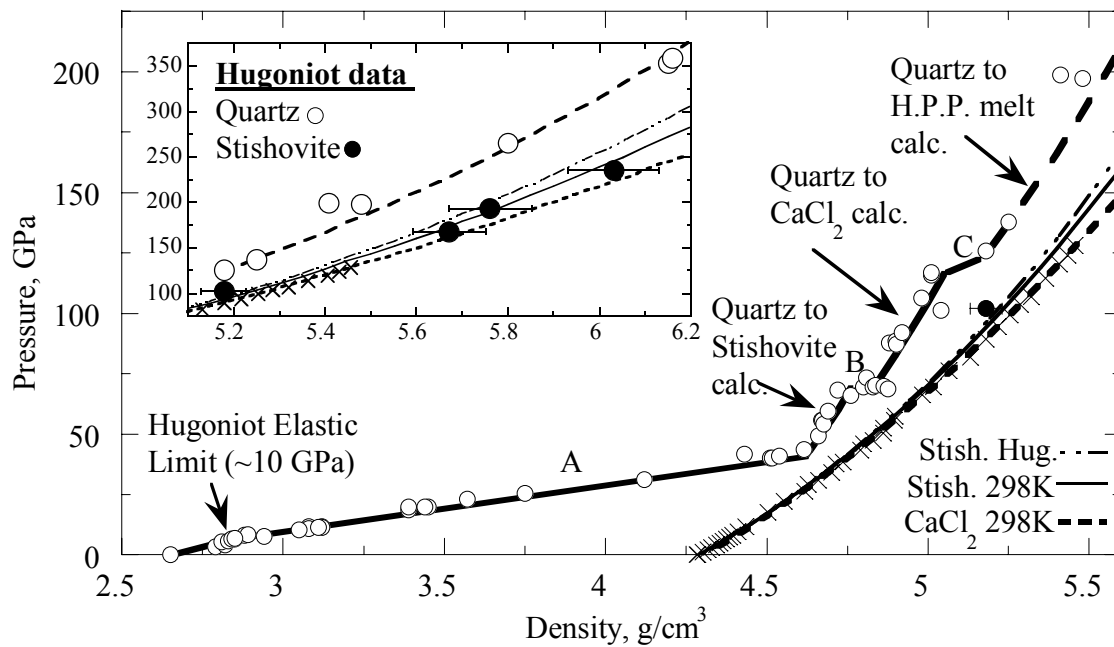
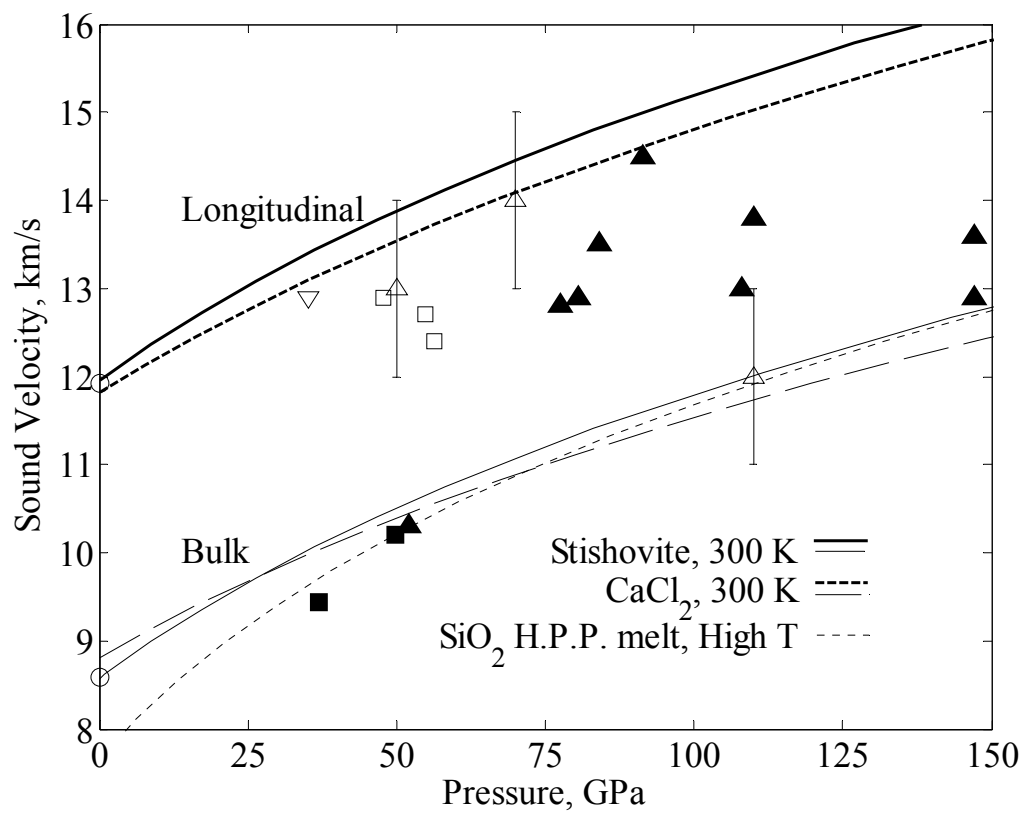


Figure 3.2 a) Sound speed measurements in SiO₂ phases with $\rho_0 = 2.65 \text{ g/cm}^3$ (symbols explained in 3.2b caption) compared to calculated 300 K curves, after *Duffy and Ahrens* [1992]. **b)** Drop in V_p of quartz shocked to stishovite, due to shear softening, prior to transition to CaCl₂ structure at 70 GPa, and drop to bulk sound velocity upon melting at 115 GPa, are evident. Quartz data of *McQueen* [1991], M91, below 90 GPa are not plotted as they are discrepant with the more reliable datum of *Chhabildas and Miller* [1985], CM85. Other data shown: *Grady et al.* [1975], G75; *Morgan and Fritz* [1979], MF79, and *Weidner et al.* [1982], W82.



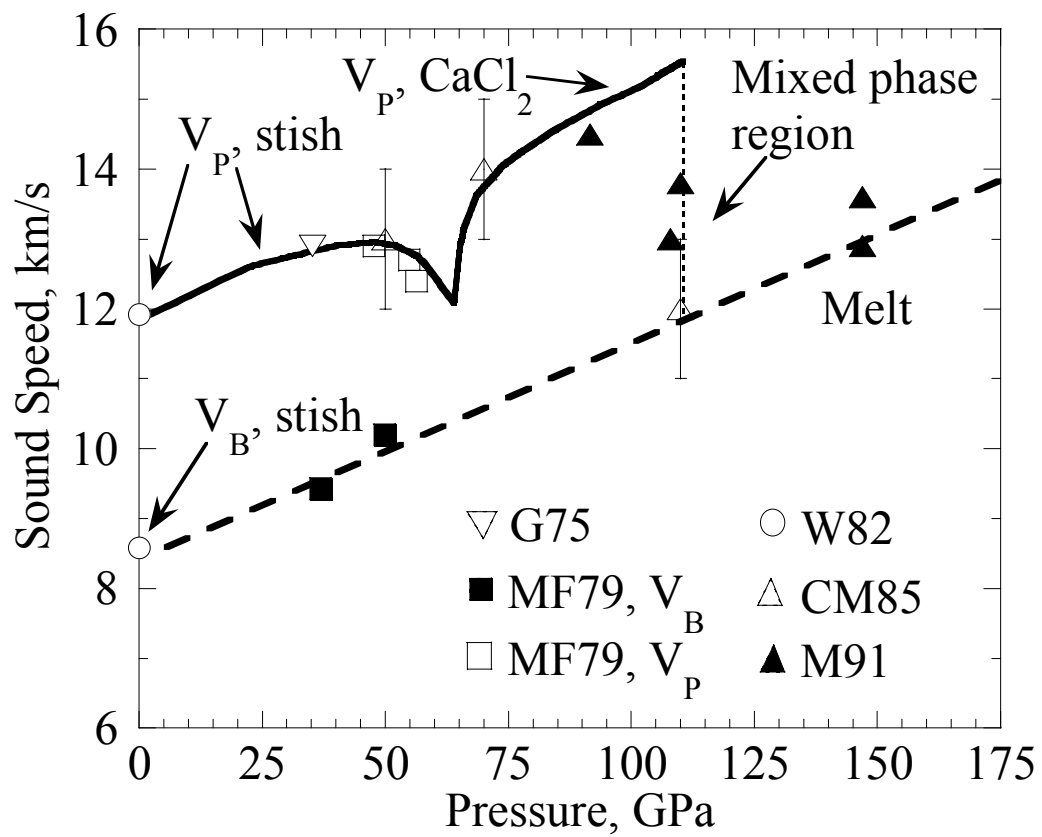


Figure 3.3 Hugoniot data on initially porous ($\rho_0 = 2.4 \text{ g/cm}^3$) [*Podurets et al.*, 1981] and zero porosity polycrystalline ($\rho_0 = 2.92 \text{ g/cm}^3$) [*Luo et al.*, 2002b; *Podurets et al.*, 1981] coesite compared to calculated Hugoniots as calculated from parameters in Tables 3.1 and 3.2.

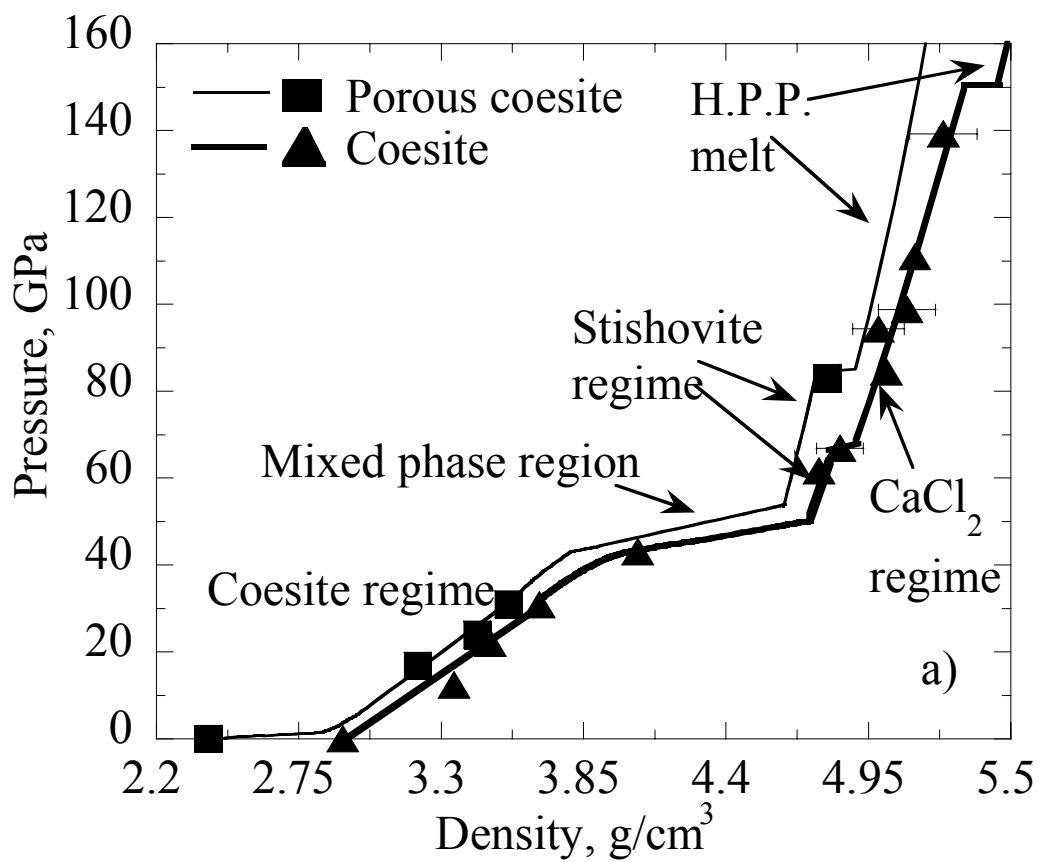


Figure 3.4 Hugoniot data on porous cristobalite ($\rho_0 = 2.13 \text{ g/cm}^3$) of [*Podurets et al.*, 1981], P81, and fused quartz ($\rho_0 = 2.2 \text{ g/cm}^3$) of [*Marsh*, 1980], M80, compared to various possible Hugoniot phases calculated from parameter values in Tables 3.1 and 3.2.

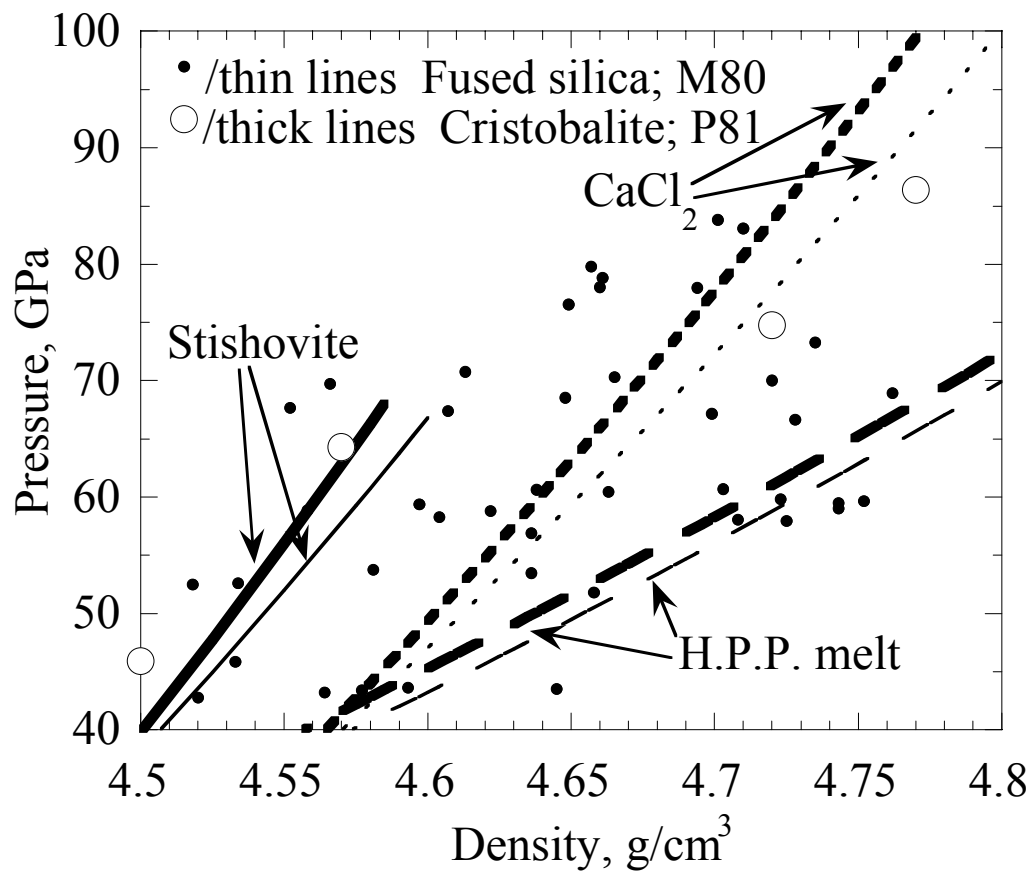


Figure 3.5 Hugoniot temperatures, fused quartz (FQ) and quartz (QTZ), of *Lyzenga et al.* [1983] (with minor corrections for Al absorption, *Boslough* [1988]) and [*McQueen and Fritz*, 1982; *Sugiura et al.*, 1982; *Wackerle*, 1962]. Melting curve, with positive slope 11 K/GPa, extrapolated from static data of *Shen and Lazor* [1995] shown for comparison. Calculated Hugoniots in melt regime: dashed curves are for $C_V = \text{constant}$ and solid curves for $C_V(T)$ from Equation 3.1.

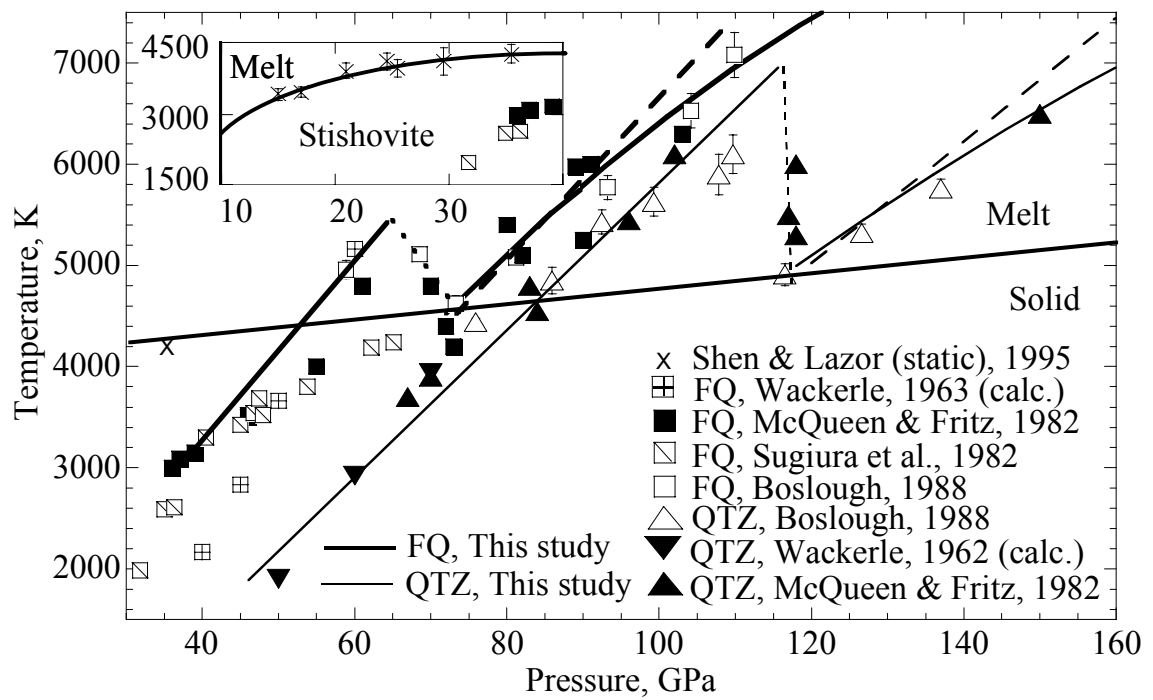
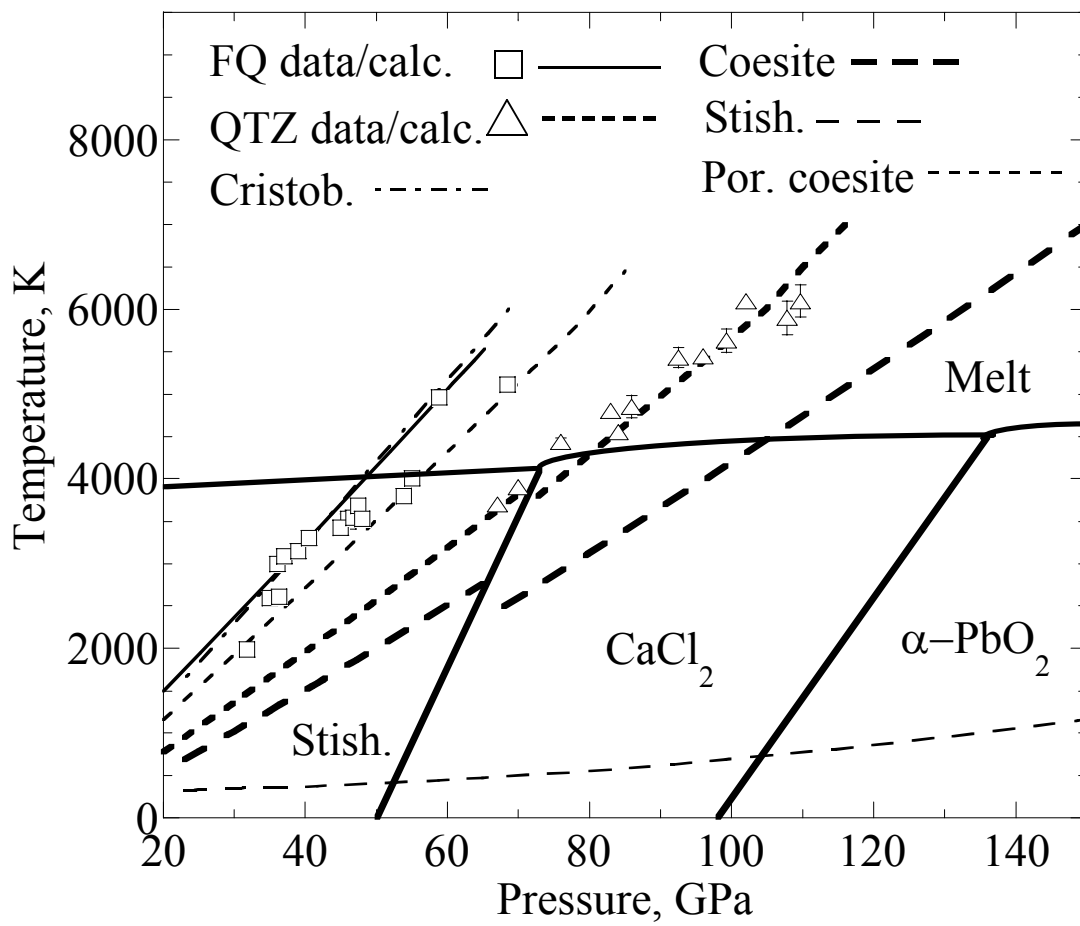
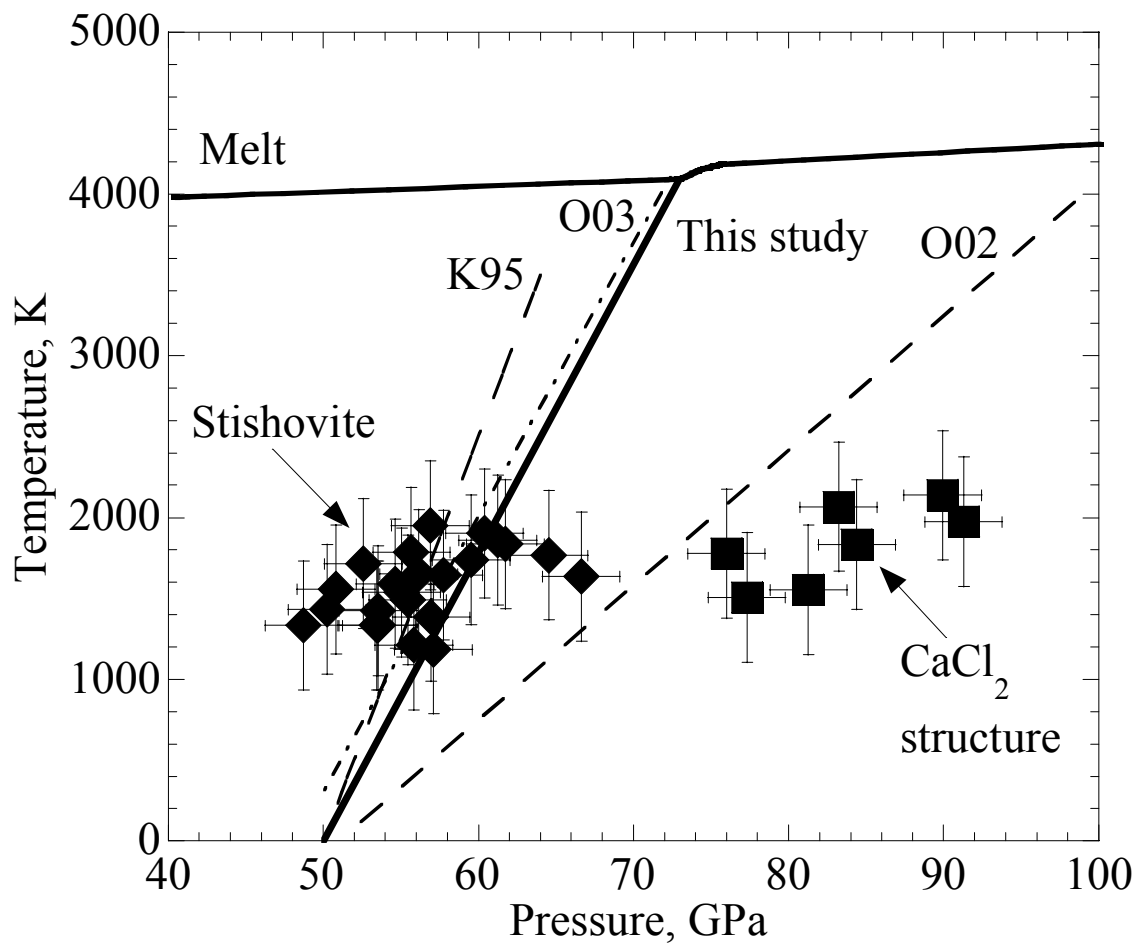


Figure 3.6 a) High pressure phase diagram of SiO_2 . Only data and calculations for solid phases are shown. Shock temperature calculations are terminated at pressures corresponding to observed, or expected, drops in temperature due to melting. The field of $\alpha\text{-PbO}_2$ [Murakami *et al.*, 2003] is shown for reference only. **b)** Additional constraints on stishovite- CaCl_2 phase boundary. K95 [Kingma *et al.*, 1995], O02 and laser heated diamond anvil data [Ono *et al.*, 2002], and O03 [Oganov *et al.*, 2003].





Chapter 4

Shock Wave Equation of State and Temperature Measurements in (Mg,Fe)SiO₃ Natural Crystal, Synthetic Glass and Porous Material

Introduction

The high pressure-temperature behavior of (Mg,Fe)SiO₃ perovskite has been a topic of intense research as it is considered the most abundant component of Earth's lower mantle [Bina, 1998]. Since the composition of perovskite in the lower mantle is thought to be ≥ 88 molecular per cent MgSiO₃ it is necessary to constrain the equation of state (EOS) and phase relations in the end member MgSiO₃ system to provide constraints on the amount of iron necessary to satisfy observations in seismology and geodynamics. Constraints on the thermal EOS of MgSiO₃ perovskite have been reported by numerous static lab and computational studies, as compiled in *Marton et al.* [2001]. Previous dynamic studies on MgSiO₃ composition are compiled in *Marsh* [1980] with additional data, up to 220 GPa, reported in *Simakov and Trunin* [1973]. This study provides further Hugoniot data up to 206 GPa on initial MgSiO₃ synthetic glass and natural crystal providing further support to existing constraints on MgSiO₃ perovskite and new insight into the behavior of MgSiO₃ melt at pressures and temperatures relevant to Earth's lower mantle.

Sample preparation

Shock wave experiments were carried out on synthetic MgSiO₃ glass and Sri Lankan enstatite. Samples of MgSiO₃ glass were prepared in E. M. Stolper's lab at Caltech, with the help of John Beckett and Michael Baker, from 99.999% pure,

devolatilized MgO (Specialty Products Lot # S20565) and 99.998% pure SiO₂ (Specialty Products Lot # 21172) mixed in an automatic agate grinder for five hours. The mixture was placed in a 10 ml Pt/5%Au crucible and heated to 1620 °C, under flowing N₂, in a vertical Deltech furnace for 18 hours, then quenched by immersing the bottom 1 cm of the crucible in a beaker of room temperature water for 10 seconds. The samples were cut to 3mm x 12mm diameter disks and polished to an optical finish. They have Archimedean densities of 2.7415 +/- 0.0027 g/cm³. The lower density of the sample used in shot 315 (Table 4.2) was due to air bubbles in the bulk sample. The target was designed such that the measured shock velocity traversed a bubble free volume of the sample.

Electron microprobe analysis of three batches is given in Table 4.1. These early attempts at synthesis did not include accounting for adsorption of H₂O during measurement of MgO mass. This resulted in the samples being enriched in Si, i.e., Si/Mg = 1.036 compared to Si/Mg = 1.000 for ideal MgSiO₃ stoichiometry. Later attempts to account for H₂O adsorption resulted in mixtures with Si/Mg ~1.000, but led to unsuccessful glassing due to formation of olivine float crystals. Additionally, wafers of the glass samples were provided to Thomas Duffy's group at Princeton to conduct perovskite synthesis experiments in the laser heated diamond cell. Successful synthesis of perovskite, along with a previously unidentified silica phase, at high pressure and temperature [Shim *et al.*, 2001] supports our present conclusion regarding the slight excess in SiO₂ of the glass samples based on the electron microprobe analysis. The slight silica enrichment in the glass samples has no obvious effect on the experimental results of this study. It appears that the ~10 ns rise time of the shock experiments is sufficient time for the majority of the glass to transform to the perovskite structure in the 50 to 100 GPa peak shock pressure

range. *Shim et al.* [2001] also confirmed that these samples have no long range order from their observation of a diffuse x-ray diffraction signal at ambient conditions.

In addition to the glass samples, several rough cut natural enstatite samples from the Embilipitiya region of Sri Lanka [*Gaminizoyisa*, 1985; *Harding et al.*, 1982], obtained from Carl Francis of Harvard University, were studied. Electron microprobe analysis indicates the samples are nearly pure magnesium end member (Table 4.1). The pyroxene composition of these samples is Wo_{0.2} En_{99.2} Fs_{0.6}, corresponding to molecular percent of the pyroxene end member components wollastonite (CaSiO₃), enstatite (MgSiO₃) and ferrosilite (FeSiO₃). Although aluminum substitution is ignored the relatively minor amounts will not alter the conclusion that these crystals are nearly pure magnesium end member enstatites. The samples used in the pressure-density equation of state (EOS) phase of this study were colorless to brownish-pink with numerous small flaws and sub-millimeter to millimeter inclusions. Samples were cut to allow streak image to sample shock behavior of the nearly flawless, and inclusion free, volumes of the crystals. This attention to detail has greatly increased the reliability of the present data set, compared to samples with higher iron content used in earlier studies, such as pyroxenites [*McQueen et al.*, 1967; *Trunin et al.*, 1965], or Bamble bronzite (En₈₅) [*Ahrens and Gaffney*, 1971; *Jeanloz and Ahrens*, 1977; *Watt and Ahrens*, 1986]. Although modern nomenclature rulings disallow the use of species designations such as bronzite for intermediate (Mg,Fe)SiO₃ pyroxene compositions [*Morimoto et al.*, 1988], the term bronzite is used in this study to refer to orthopyroxenes of composition En₇₀ to En₈₈, in keeping with the historical designation of original papers and to avoid confusion when referring to Sri Lankan enstatite and synthetic glass which are referred to as En₁₀₀ for simplicity.

Experimental results

A total of fourteen shock wave pressure-density equation of state (EOS) experiments were conducted; eleven on enstatite and three on synthetic glass samples. Results are listed in Table 4.2. A single shock temperature measurement was carried out on a glass specimen shocked to 107 ± 4 GPa. The measured temperature was 5050 ± 173 K with an emissivity of 0.78 ± 0.13 as outlined in Chapter 2. In all experiments copper, aluminum, or tantalum flyer plates were accelerated to impact speeds up to 7.38 ± 0.01 km/s using a 25mm two-stage light gas gun [Jeanloz and Ahrens, 1977]. Pressures were calculated by the impedance match method [Ahrens, 1987] using standard equations of state for Al, Cu and Ta [Mitchell and Nellis, 1981]. Impactor speed was measured by the flash x-ray method. Bowing and tilting of the flyer was accounted for using techniques outlined in Jeanloz and Ahrens [1980].

Dynamic Compression of Amorphous, Porous and Crystalline (Mg,Fe)SiO₃: Interpretation

Theoretical Hugoniot pressure-density and pressure-temperature curves for MgSiO₃ crystal and synthetic glass based on the Mie-Grüneisen offset from the 3rd order Birch-Murnaghan isentropes for each high pressure phase (H.P.P.) as outlined in Chapter 2 were calculated. Parameter values for each phase are listed in Tables 4.3 and 4.4. Based on these calculations, the phase diagram of Figure 4.3, the independent pressure-density and pressure-temperature Hugoniot data for the two MgSiO₃ phases studied in this work, and the data of [Ahrens and Gaffney, 1971; Jakubith and Hornemann, 1981; Jeanloz and Ahrens, 1977; Marsh, 1980; Simakov and Trunin, 1973; Trunin et al., 1965; Watt and Ahrens, 1986] the following ten regimes along the (Mg,Fe)SiO₃ Hugoniot are inferred (Figure 4.1): 1) The elastic shock Hugoniot extending to 6.7 GPa [Ahrens and Gaffney,

1971]. 2) The enstatite deformational Hugoniot from 6.7 to 15 GPa. 3) Mixed phase regime (A) of enstatite and majorite extending from 15 to 34 GPa [Ahrens and Gaffney, 1971]. 4) The majorite regime from 34 to 48 GPa [Ahrens and Gaffney, 1971]. 5) Mixed phase regime (B) of majorite and akimotoite (ilmenite structure) from 48 to 70 GPa. 6) The akimotoite regime from 70 to 105 GPa. 7) Mixed phase regime (C) of akimotoite and perovskite structure from 105 to 110 GPa. 8) The perovskite structure regime from 110 to ~170 GPa. 9) Mixed phase regime (D) of perovskite and melt in the 170 to 175 GPa range. 10) The melt regime > 175 GPa. The remainder of this section provides support for this interpretation of the Hugoniot data, and further insight into the observed behavior of the data presented in Figure 4.1, i.e., $\Delta V_m = V_{\text{melt}} - V_{\text{solid}} > 0$ at 30 GPa and < 0 at 170 GPa.

Mixed Phase Regime

The Hugoniot Elastic Limit (H.E.L.) and mixed phase regime up to 48 GPa were previously studied in Bamble bronzite [Ahrens and Gaffney, 1971]. In the present study EOS shots with peak shock pressures of 48.2 ± 2.1 , 57.4 ± 2.1 and 68.1 ± 2.4 GPa show evidence of first arrivals that lead to a partial loss of reflectivity in the mirrors followed by a second shock that completely extinguishes reflectivity. The average wave velocity of the precursor is 9.10 ± 0.52 km/s. Since the shock and particle velocities must be known to calculate pressure (Equation 2.2), and using only flat mirrors it is possible to determine only the shock velocity, it is not possible to determine the pressure corresponding to the precursors in this study. The impedance match method provides the particle velocity at peak shock conditions only (Figure 2.2).

The average longitudinal sound velocity of Sri Lankan enstatite measured prior to these experiments is listed in Table 4.5 along with sound velocities in Bamble bronzite, and related high pressure phases. Precursor velocities are listed for comparison. The velocity measurements were made in G. Ravichandran's lab at Caltech using ultrasonic transducers. It is a reasonable conclusion of *Ahrens and Gaffney* [1971] that the initial arrival in Bamble bronzite, up to 48 GPa peak pressure, is an elastic shock propagating in unshocked crystal, as the longitudinal elastic wave and elastic shock have similar velocities (Table 4.5). For enstatite, however, the observed first arrival average velocity of 9.1 km/s is greater than the maximum measured longitudinal elastic velocity. It is possible that the first arrival is a transition wave related to formation of majorite in the rising shock, whose ambient longitudinal elastic velocity is 8.9 km/s. Complete conversion to majorite should lead to stiffening of the Hugoniot at ~ 50 GPa, in excellent agreement with the calculated enstatite to majorite Hugoniot (Figure 4.2), however, the majorite transition wave is followed by a transition to the akimotoite structure. Not until 70 GPa does the akimotoite transition wave overtake all precursors and the Hugoniot stiffens due to complete conversion to akimotoite in good agreement with the calculated Hugoniot (Figure 4.2).

No precursor was observed in MgSiO_3 glass shocked to a peak pressure of 47 GPa in the present study. Sound velocities in the glass samples were not measured before the experiments due to excessive noise in transducer signals. No observation of precursors, or sound velocities, was reported in *Marsh* [1980] for the porous MgSiO_3 data in Figure 4.2. It is reasonable to assume that any elastic waves generated in the shock front of these samples would be much slower than those in the crystal and easily overtaken by the peak shock wave. The 47 GPa peak pressure is in the proposed majorite single phase regime,

therefore no two-wave shock structure is expected. Differences in phases achieved along different Hugoniot due to varying iron content and isobaric temperature differences along Hugoniot of varying initial porosities are not analyzed here. A detailed study of these effects requires much more work and is left to others.

Shock recovery experiments of *Jakubith and Hornemann* [1981] on Bamble bronzite in the peak shock pressure range of 10 to 50 GPa show x-ray evidence of bronzite up to 25 GPa and a mixture of bronzite, clinoenstatite and majorite recovered from peak shock pressures in the 25 to 50 GPa range. Strong majorite diffraction lines are found only in material recovered from > 40 GPa peak pressure. The recovered bronzite observed in these shots may be due to reversion from majorite prior to x-ray analysis. These findings are consistent with the interpretation of the pressure-density Hugoniot data presented in Figure 4.1. The results of *Jakubith and Hornemann* [1981] need to be verified, as it is possible that weathering impurities in the Bamble bronzite led to regions of melt in the samples that would not occur in a more pure gem quality material such as Sri Lankan enstatite. Additional support of the conversion of enstatite to H.P.P. under shock conditions is evidence of majorite, akimotoite, ringwoodite, and perovskite observed in shock-induced melt veins of several chondritic meteorites [*Chen et al.*, 1996; *Sharp et al.*, 1997; *Smith and Mason*, 1970; *Stöffler*, 1997]. The Hugoniot P-V-T states achieved by these phases will be discussed later.

Calculated High-Pressure Phase Hugoniot

In the pressure range of 70 to 105 GPa, shown in Figure 4.1 and in detail in Figure 4.2, it is clear the enstatite Hugoniot data are less dense than predicted for conversion to perovskite. The datum plotted in Figure 4.1 from *Fiquet et al.* [2000] laser heated to 2900

K in the diamond anvil cell, confirmed to be in the perovskite structure by X-ray diffraction, is ~ 1400 K hotter and more dense than the enstatite Hugoniot supporting the assertion that a less dense phase than perovskite is attained along the 70 to 105 GPa region of the enstatite Hugoniot.

The possibility of an overdriven phase transition to a phase stable < 25 GPa under static equilibrium conditions is investigated. Calculated Hugoniots of possible high pressure phases are shown in Figure 4.2. From these calculations, akimotoite is the most likely phase attained along this segment and is consistent with the phase progression with increasing pressure observed in static phase equilibria experiments. The Hugoniot for a mixture of periclase and stishovite is only slightly more dense than the data, but is not consistent with recent static experiments at relevant pressures [Serghiou *et al.*, 1998; Shim *et al.*, 2001]. The breakdown of the perovskite structure to its component oxides was observed by Meade *et al.* [1995] and Saxena [1996], though Serghiou *et al.* [1998] found only perovskite and no evidence of the component oxides using Raman spectroscopy on material recovered from the same pressure range. Shim *et al.* [2001] concluded perovskite is stable over the 50 to 106 GPa and 1600 to 2400 K range based on in situ observations using more recent technical improvements to decrease thermal and stress gradients in the diamond cell. The stability of perovskite over mixed oxides is also supported by the Gibbs Free Energy calculations of Luo *et al.* [2002b].

Figure 4.3 shows calculated Hugoniot temperatures as a function of pressure for enstatite shocked to various high-pressure phases using the parameters listed in Tables 4.3 and 4.4. The assumption that the specific heat, C_V , is equal to a constant $3nR$ is only valid above the Debye temperature which is not well constrained for many of the phases used in

the calculations. Since the specific heat may be overestimated in the calculations the temperatures may be underestimated (Equation 2.19); however, it is interesting to note that, except for ringwoodite + stishovite and perovskite, Hugoniot temperatures are ~ 1000 K less than the corresponding equilibrium phase region. Assuming a phase at any pressure will not form at temperatures colder than its equilibrium stability field, the interpretation that majorite is formed at peak shock pressures along the $(\text{Mg,Fe})\text{SiO}_3$ crystal Hugoniot requires an increase in temperature of over 1500 K. It is proposed that frictional energy generated by shear banding, as observed in quartz [Brannon *et al.*, 1983], provides the needed heat.

The observation of high pressure phases found only in shock veins of meteorites, mentioned earlier, argues in favor of the suggestion that high-pressure phases crystallize from the melt. By implication they also form when the melt is still at elevated pressure, during adiabatic release from the peak shock state as proposed by Ringwood [1975]. His conclusion that the majorite crystallized from the melt was based on minor element differences in the composition of the majorite and unshocked orthopyroxene of the Coorara meteorite. Additional support of his conclusion is that no majorite observed in shocked veins shows evidence of tetragonal symmetry (low temperature majorite), twinning, or tweeds, observed in cubic majorite quenched in lab experiments. Based on these observations and quench rates Tomioka *et al.* [2002] conclude that cubic majorite observed in shock veins cooled more rapidly than 1000°C/s , consistent with adiabatic cooling from the peak shock state. In this regard, labeling the 34 to 48 GPa segment of the Hugoniot as the majorite regime is incorrect, as it is not formed uniformly in the sample at peak shock pressures, but more likely due to release from bands, or pockets, of melt. The shock

temperature calculations support the presence of ringwoodite + stishovite in the 34 to 48 GPa region, however, there is no reported evidence of their presence in the recovered lab samples of *Jakubith and Hornemann* [1981].

Melting of MgSiO₃ Perovskite: Constraints on the Melting Curve at High Pressures

Based on calculated high pressure phase Hugoniots (Figure 4.4), the high pressure regime along the Hugoniot of enstatite, in the 110 to 170 GPa range, is highly concordant with diamond anvil [*Fiquet et al.*, 2000] and Brillouin scattering [*Yeganeh-Haeri*, 1994] based EOS data for MgSiO₃ perovskite structure. The density jump at ~ 170 GPa is not consistent with any known solid-solid phase transition. Based on calculated Hugoniots the absolute and relative densities of the transition are too large for it to be due to the solid-solid breakdown of the perovskite structure to MgO + SiO₂ (CaCl₂ structure), or MgO + SiO₂ H.P.P. melt (Figure 4.4). It is therefore proposed that it is due to the complete transition to MgSiO₃ H.P.P. melt along the Hugoniot. A similar jump is observed along the Hugoniot of quartz at 115 GPa with a corresponding drop in longitudinal sound velocity from 15.5 km/s to the bulk sound velocity of 12 km/s and a drop in temperature from 7000 K in the solid to 5000 K in the liquid as discussed in Chapter 3. The SiO₂ sound velocity data indicate the bulk sound velocity of the melt at high pressure and temperature is similar to that of the solid at high pressure and room temperature (Figure 3.2). Assuming similar behavior for magnesium silicates, the EOS of H.P.P. MgSiO₃ melt should have a bulk sound velocity similar to that of perovskite at 300 K and pressures of 100 to 200 GPa.

Based on expected behavior similar to quartz (Figure 3.5), at 170 GPa where the proposed transition to the melt is observed in pressure-density for the MgSiO₃ crystal (Figure 4.1), the Hugoniot temperature curve should cross the melting curve. As there are

no constraints on the melting curve of MgSiO₃ at pressures greater than 85 GPa (Figure 4.3), three possibilities will be explored: a smooth extrapolation of *Sweeney and Heinz's* [1998] positively sloped, ~1.7 K/GPa at pressures greater than 50 GPa, Simon equation (Figure 4.3) designated Simon (SH98); a turnover to a negative slope along the SH98 extrapolation at 95 GPa designated curve G-C (discussed later); and a third possibility of a steeper slope, ~30 K/GPa, attaining a melting temperature of ~ 5500 K at 100 GPa preferred by *Boehler* [2000] with a subsequent turnover to a negative slope at ~ 100 GPa designated curve G'-C' (discussed later).

Given the expected cooler temperature of the melt at 170 GPa, due to superheating of the solid prior to melting, it is necessary to address the possibility that the density difference is due solely to thermal effects and not compressibility. Assuming a high compression thermal expansion coefficient for MgSiO₃ perovskite of $1 \times 10^{-5} \text{ K}^{-1}$ [*Anderson*, 1995] and a temperature difference of 1200 K based on extrapolation of the *Sweeney and Heinz* [1998] melting curve to 170 GPa (thin dashed curve in Figure 4.5a), twice the pressure of their highest data, accounts for only a 1 % density increase in the solid at 170 GPa. Based on these observations the present analysis indicates MgSiO₃ melt is 2-3% denser than the solid at pressures and temperatures corresponding to the lower 1000 km of the mantle. This supports the possibility of the presence of a significant fraction of partial melt in the ULVZ observed by seismology and warrants more detailed analysis.

An additional implication of the melt being denser than the solid is a negative slope for the melt boundary based on the Clapeyron equation

$$\partial T / \partial P = \Delta V_m / \Delta S_m, \quad (4.1)$$

where $\Delta V_m = V_{\text{melt}} - V_{\text{solid}}$ and the change in entropy is $\Delta S = S_{\text{melt}} - S_{\text{solid}}$. Since there are no known instances of $\Delta S < 0$ upon melting, it is assumed that $\Delta S > 0$. Given $\Delta V_m < 0$ yields a negative Clapeyron slope. A negative Clapeyron slope is inconsistent with a smooth extrapolation of the *Sweeney and Heinz* [1998] melting curve to pressures greater than 100 GPa.

Using the bulk sound velocity constraint mentioned earlier and the transition of the *Sweeney and Heinz* [1998] melting curve to a negative slope a H.P.P. melt EOS was developed. Temperature calculations for glass and enstatite shocked to perovskite and H.P.P. melt, designated H.P.P. melt1 (Tables 4.3 and 4.4), are shown in Figure 4.5a. The turnover to a negative sloped Clapeyron curve at 95 GPa is discussed below. In Figure 4.5b Hugoniot temperature calculations for MgSiO_3 glass and crystal shocked to perovskite, and subsequently to melt, are shown accounting for the higher temperature melting curve of *Boehler* [2000]. The EOS used in this case is denoted H.P.P. melt2 (Tables 4.3 and 4.4). It was not possible to simultaneously satisfy the constraint that the bulk sound velocity of the liquid is similar to that of the solid at high compression and 300 K, and a negative Clapeyron slope, in developing an EOS for H.P.P. melt2. The bulk sound velocity of H.P.P. melt2 is ~10 % less than that calculated for H.P.P. melt1 in the 100 to 200 GPa range.

The slope of the melting curve may be calculated by a finite difference calculation of the left side of Equation 4.1 using the intersections of the proposed melting curve with the glass and crystal H.P.P. melt segments at 123 and 170 GPa, points G and C in Figure 4.5a, respectively. This indicates a Clapeyron slope of -10 K/GPa. With this slope, a calculated density of the solid (perovskite) along the melt boundary at 170 GPa of 5.5

g/cm^3 , and a 2.5 % density increase upon melting, ΔS is constrained to be 1.1R. This value of ΔS is similar to the 1.3R value constrained by *Lyzenga et al.* [1983] along the positive slope melt boundary of 11 K/GPa in the high pressure regime of the SiO_2 system. A similar analysis along the higher melting temperature curve of Figure 4.5b, between points G' and C', yields a Clapeyron slope of -16 K/GPa.

For a given thermal expansion a larger temperature difference between the super heated solid and the melt will result in a larger thermal correction of the density jump at 170 GPa, and therefore, a smaller $\Delta V_m = V_{\text{melt}} - V_{\text{solid}}$. Since the thermal expansion of perovskite at high pressures and temperatures is not known the trade off between thermal expansion and temperature drop was investigated using the equation

$$V_s = V_{\text{SHS}} [1 + \alpha(T_{\text{melt}} - T_{\text{SHS}})]. \quad (4.2)$$

Subscript SHS refers to volume, V, and temperature, T, of super heated solid (SHS) at 170 GPa. Subscript melt refers to the calculated Hugoniot state of the melt at 170 GPa. Figure 4.6 summarizes the results of the calculations. The points marked Simon, G-C and G'-C' are defined in Figures 4.5a and b and the values listed in Table 4.6. Since compression counteracts thermal expansion, it is unlikely that the thermal expansion of the super heated perovskite at 170 GPa and ~5000 K is much greater than the $2.7 \times 10^{-5} \text{ K}^{-1}$ at 5000 K and room pressure calculated from $\alpha(T) = 2.18 \times 10^{-5} \text{ K} + (T_2 - T_1) \times 0.11 \times 10^{-8} \text{ K}^{-2}$, constrained by *Fiquet et al.* [2000]. It is also reasonable to assume the thermal expansion of the perovskite is similar to that of MgO, $\sim 1.5 \times 10^{-5} \text{ K}^{-1}$, in the 170 to 200 GPa region constrained by shock wave experiments [*Speziale et al.*, 2001].

Assuming the jump in density observed at 170 GPa along the MgSiO₃ crystal Hugoniot is due to melting, the positively sloped melting curve of *Sweeney and Heinz* [1998] would require a larger thermal expansivity at 170 GPa than at room pressure (closed circle compared to vertical dashed line in Figure 4.6). Such behavior may be the result of the solid being in a super heated metastable state. A negative deviation from the *Sweeney and Heinz* [1998] melting curve above 100 GPa, as shown in Figure 4.5a, would result in a larger drop in temperature up to an assumed maximum of 2000 K. Again within uncertainty it is unlikely that the melt is less dense than the solid, e.g., the melting curve does not have a positive slope above 100 GPa. The steeper melting curve presented in Figure 4.5b results in a smaller temperature difference. It is unlikely the temperature in the melt would be greater than the solid, so the tip of the crystal to perovskite temperature calculation at 170 GPa places a constraint on the melting temperature of ~ 5500 K. *Boehler's* [2000] data up to 58 GPa extrapolates smoothly into this point with a positive slope. This is inconsistent with the density jump observed at 170 GPa along the Hugoniot of MgSiO₃ crystal (Figure 4.1). From Figure 4.6 it is obvious that small temperature differences between the super heated perovskite and melt, ~ 500 K, would require thermal expansivities approaching 10^{-4} K^{-1} for even a weakly positive slope melting curve. If the steeper melting curve is accurate the Hugoniot data presented in this study require a drastic turnover in the melting curve at ~ 100 GPa such that the slope is negative in the 150 to 200 GPa range.

In contrast with the melting behavior at high pressure is the Hugoniot data for an ultraporous mixture of MgO and fused silica, $\rho_0 = 1.58 \text{ g/cm}^3$, to nearly 50 GPa plotted in Figure 4.1. At 30 GPa the data exhibit an abrupt decrease in density of $\sim 10\%$.

Calculations of possible H.P.P. indicate only perovskite is dense enough to account for the density of 4.2 g/cm^3 achieved at 30 GPa (Figure 4.2). The corresponding temperature is 4000 K, above the melting curve of MgSiO_3 at 30 GPa (Figure 4.3). It is proposed that the density decrease is due to melting, as would be expected. This is in contrast to the increase in density observed upon melting at 170 GPa along the Hugoniot of the crystal. Calculated pressure-density and pressure-temperature Hugoniots for ultraporous $\text{MgO} + \text{SiO}_2$ shocked to enstatite melt, using parameter values similar to those for diopside melt [Rigden *et al.*, 1989], show remarkable agreement with the pressure-density data (Figure 4.2) and superheated behavior relative to the melting curve constrained by static experiments (Figure 4.3).

Figure 4.7 demonstrates a long standing discrepancy in the $(\text{Mg,Fe})\text{SiO}_3$ Hugoniot data. The bifurcation in the data at 60 GPa, when compared to the magnesium end member data of Figure 4.1, appears to have a subset of samples that reaches higher density than predicted for conversion to perovskite. It is proposed that these samples have been shocked to partial, or complete, melt states. This is attributed to impurities in the pyroxenite samples, and weathering of the Bamble bronzite. This conclusion is supported by the observation of Sweeney and Heinz [1998] that Bamble bronzite melts at temperatures up to 1500 K less than Webster bronzite, or synthetic enstatite.

Conclusions

Based on the preceding analysis of Hugoniot data for $(\text{Mg,Fe})\text{SiO}_3$ composition the following conclusions are drawn:

- 1) With increasing pressure, complete transition to akimotoite, perovskite and H.P.P. melt occurs along the Hugoniot of $(\text{Mg,Fe})\text{SiO}_3$.

- 2) The change in volume upon melting of MgSiO_3 is positive at low pressures, but becomes negative at pressures greater than 100 GPa, e.g., the melt is 2-3 % denser than the solid.
- 3) Recovered high pressure phases are due to adiabatic cooling of melt formed in shear bands in pure phases, or melt pockets nucleated due to impurities.
- 4) Purity of samples is of previously unappreciated importance in studying the high pressure Hugoniot behavior of silicates. The bifurcation in previous Hugoniot data collected on $(\text{Mg,Fe})\text{SiO}_3$ samples is due to partial, or complete melting.

Table 4.1: Electron microprobe analysis of MgSiO₃ synthetic glass and natural enstatite. Molar analysis based on six oxygens.

Element	Synthetic glass (This study) ^{a)}	Sri Lankan Enstatite (This study) ^{b)}	Sri Lankan Enstatite ^{c)}
Si	2.022 ± 0.003	1.984 ± 0.003	1.98
Al	< 0.001	0.060 ± 0.001	0.067
Ti	< 0.001	0.001 ± 0.000	0.001
Fe	< 0.001	0.010 ± 0.001	0.028
Mg	1.952 ± 0.005	1.924 ± 0.005	1.904
Ca	< 0.001	0.004 ± 0.000	0.004
Na	0.002 ± 0.001	-	0.001
Si/Mg	1.036	1.031	1.04

^{a)} Based on a total of 17 analysis points in 3 glass samples. ± 1 s.d.

^{b)} Based on a total of 5 analysis points in 1 sample. ± 1 s.d.

^{c)} *Gaminizoysa* [1985]

Table 4.2: Enstatite natural crystal and synthetic glass shock wave data. * Denotes 2nd arrival. Uncertainties in last one, or two, figures shown in parentheses.

Shot Number	Initial Density, ρ_o (g/cm ³)	Flyer/Driver	Flyer Velocity, U_{fp} (km/s)	Shock Velocity, U_s (km/s)	Hugoniot Pressure, P_h (GPa)	Hugoniot Density, ρ_h , (g/cm ³)
<u>Glass</u>						
315	2.712(5)	Al/Al	4.51(1)	7.24(7)	47.1(7)	4.06(3)
313	2.743(5)	Cu/Cu	5.05(1)	8.53(6)	83.1(6)	4.70(3)
312	2.740(5)	Cu/Cu	6.07(1)	9.49(13)	110.0(16)	4.94(6)
<u>Crystal</u>						
328	3.195(5)	Al/Al	4.16(1)	9.30(30) 7.50(12)*	- 48.2(21)	- 4.37(7)
320	3.121(5)	Al/Al	4.56(1)	9.35(25) 7.78(16)*	- 53.9(20)	- 4.37(7)
327	3.209(5)	Al/Al	5.34(1)	8.64(35) 8.22(4)*	- 68.1(28)	- 4.68(11)
317	3.167(5)	Cu/Cu	4.62(1)	9.13(6)	88.2(7)	4.75(2)
326	3.166(5)	Cu/Cu	5.44(1)	9.65(4)	110.0(6)	5.05(2)
316	3.227(5)	Cu/Cu	5.71(1)	10.06(7)	121.4(10)	5.14(3)
321	3.197(5)	Ta/Ta	5.98(1)	10.79(3)	149.4(7)	5.34(2)
324	3.173(5)	Ta/Ta	6.52(1)	11.34(6)	169.8(11)	5.44(3)
318	3.225(5)	Ta/Ta	6.71(1)	11.16(9)	175.3(15)	5.72(4)
322	3.192(5)	Ta/Ta	7.22(1)	11.69(5)	195.5(10)	5.79(2)
319	3.242(5)	Ta/Ta	7.38(1)	11.99(19)	206.4(35)	5.82(8)

Table 4.3: Elastic Parameter Values for MgO, MgSiO₃, and Mg₂SiO₄ Compositions.

Phase	Initial Density, ρ_0 (g/cm ³)	Bulk Modulus, K_0 (GPa)	$d K_0 / dP$, K'
<u>Mg₂SiO₄ Composition</u>			
Wadsleyite	3.474 ^{a)}	174 ^{a)}	4.4 ^{b)}
Ringwoodite	3.559 ^{c)}	190 ^{d)}	4.19 ^{d)}
<u>MgSiO₃ Composition</u>			
Enstatite	3.22 ^{e)}	108 ^{g)}	6.0 ^{h)}
Enstatite melt	2.57 ⁿ⁾	29 ^{p)}	6.9 ^{o)}
Majorite	3.522 ^{f)}	162 ^{f)}	6.7 ^{f)}
Akimotoite	3.795 ⁱ⁾	212 ⁱ⁾	4 ^{e)}
Perovskite	4.103 ^{j)}	260 ^{j)}	3.7 ^{j)}
Wadsleyite + Stishovite ^{k)}	3.668 ^{m)}	203 ^{m)}	4.5 ^{m)}
Ringwoodite + Stishovite ^{k)}	3.737 ^{m)}	217 ^{m)}	4.3 ^{m)}
Periclase + Stishovite ^{k)}	3.956 ^{m)}	234 ^{m)}	4.6 ^{m)}
Periclase + CaCl ₂ (SiO ₂) ^{k)}	3.981 ^{m)}	228 ^{m)}	4.6 ^{m)}
H.P.P. melt1	4.000 ^{e)}	160 ^{e)}	6.0 ^{e)}
H.P.P. melt2	3.95 ^{e)}	145 ^{e)}	4.5 ^{e)}
Periclase + SiO ₂ H.P.P. melt ^{k)}	3.865 ^{m)}	202 ^{m)}	5.1 ^{m)}
<u>MgO</u>			
Periclase	3.580 ^{l)}	162 ^{l)}	4.13 ^{l)}

a) Bass [1995].

b) Li and Liebermann [2000].

c) Jackson et al. [2000].

d) Kiefer et al. [1997].

e) This study (see text).

f) Gwanmesia et al. [2000].

g) Weidner et al. [1978].

h) Webb and Jackson [1993].

i) Weidner and Ito [1985].

j) Fiquet et al. [2000].

k) Table 3.1.

l) Jackson and Niesler [1982].

m) Voigt-Reuss-Hill averages [Watt et al., 1976].

n) Lange and Carmichael [1987].

o) Rigden et al. [1989].

p) Diopside melt $K_0 = 22.4$ GPa ^{o)}.

Table 4.4: Thermodynamic Parameter Values for MgO, MgSiO₃, and Mg₂SiO₄ Compositions.

Phase	Gruneisen Parameter, γ_o^a	q^a	Transition Energy, E_{tr}^b (MJ/kg)	C_v^c , (J/kg K)
			From forsterite	
<u>Mg₂SiO₄ Composition</u>				
Wadsleyite	1 ^{d)}	1 ^{d)}	0.30 ^{e)}	3nR ^{d)}
Ringwoodite	1.24 ^{f)}	1 ^{d)}	0.40 ^{e)}	3nR ^{d)}
			From enstatite	
<u>MgSiO₃ Composition</u>				
Enstatite	0.88 ^{g)}	1 ^{d)}	-	-
Enstatite melt	0.3 ^{h)}	1 ^{d)}	1.0 ^{d)}	0.85*3nR ^{d)}
Majorite	1 ^{d)}	1 ^{d)}	0.36 ^{e)}	3nR ^{d)}
Akimotoite	1.24 ⁱ⁾	2 ^{d)}	0.59 ^{e)}	3nR ^{d)}
Perovskite	1.5 ^{j)}	0.5 ^{d),k)}	1.10 ^{e)}	1.05*3nR ^{d)}
Wadsleyite + Stishovite ^{o)}	1.1 ^{l)}	1 ^{l)}	0.15 ^{e)}	3nR ^{d)}
Ringwoodite + Stishovite ^{o)}	1.3 ^{l)}	1 ^{l)}	0.25 ^{e)}	3nR ^{d)}
Periclase + Stishovite ^{o)}	1.4 ^{l)}	1 ^{l)}	1.0 ^{e)}	3nR ^{d)}
Periclase + CaCl ₂ (SiO ₂) ^{o)}	1.5 ^{l)}	1 ^{l)}	1.5 ^{d)}	3nR ^{d)}
H.P.P. melt1	0.8 ^{d)}	1.6 ^{d)}	1.80 ^{d)}	1.1*3nR ^{d)}
H.P.P. melt2	2.1 ^{d)}	1 ^{d)}	2.1 ^{d)}	1.1*3nR ^{d)}
Periclase + SiO ₂ H.P.P. melt ^{o)}	0.8 ^{l)}	1.5 ^{l)}	1.6 ^{o)}	3nR ^{d)}
<u>MgO</u>				
Periclase	1.52 ^{m)}	1 ^{m)}	-	3nR ⁿ⁾

a) $\gamma = \gamma_o (V/V_o)^q$ b) $E_{tr} = \Delta E \cong \Delta H$ at zero pressure.c) $n = \#$ of atoms per formula unit.

d) This study.

e) Navrotsky [1995].

f) Piekartz et al. [2002].

g) Yang and Ghose [1994].

h) Rigden et al. [1989].

i) Reynard and Rubie [1996].

j) Stixrude and Bukowinski [1993].

k) For $K' = 4$, $q = 1$.

l) Voigt-Reuss-Hill averages [Watt et al., 1976].

m) Duffy [1992].

n) Svendsen and Ahrens [1987].

o) Table 3.2.

Table 4.5: Wave velocities

Phase	Ambient Longitudinal Sound Velocity, V_p (km/s)	Observed Peak Shock Pressure Range (GPa)	Peak Shock Precursor Velocity (km/s)
Bamble bronzite ^{a)}	7.865 ± 0.015	15 – 48 GPa	7.78
Sri Lankan enstatite ^{b)}	8.41 ± 0.31	48 – 68 GPa	9.10 ± 0.52
Majorite ^{c)}	8.90	-	-
Ringwoodite ^{d)} + Stishovite ^{d)}	$10.4^e)$	-	-
Wadsleyite ^{d)} + Stishovite ^{d)}	$10.2^e)$	-	-
Akimotoite ^{f)}	10.11	-	-

^{a)} *Ahrens and Gaffney* [1971].

^{b)} This study (see text).

^{c)} *Gwanmesia et al.* [2000].

^{d)} *Bass* [1995].

^{e)} Voigt-Reuss-Hill average [*Watt et al.*, 1976].

^{f)} *Weidner et al.* [1985].

Table 4.6: Constraints on Clapeyron slope of melting curves at P = 170 GPa.

Melting curve	dT/dP	ΔS ^{a)}	$\Delta V_m/V_s$	$\alpha_{\text{perovskite}}$	ΔT
Simon (SH98) ^{b)}	1.7 K/GPa	1.1R	0.5 %	$3.9 \times 10^{-5} \text{ K}^{-1}$	-1200 K
G-C ^{c)}	-10 K/GPa	1.1R	-2.5 %	$1.0 \times 10^{-5} \text{ K}^{-1}$	-2000 K
G'-C' ^{d)}	-16 K/GPa	1.1R	-4.0 %	$1.0 \times 10^{-5} \text{ K}^{-1}$	-450 K

^{a)} $R = 415 \text{ J/kg K}$.

^{b)} Extrapolation of *Sweeney and Heinz's* [1998] Simon equation.

^{c)} $\Delta V_m < 0$ assuming shallow slope of SH98 up to 100 GPa (Figure 4.5a).

^{d)} $\Delta V_m < 0$ assuming steeper slope of *Boehler* [2000] up to 100 GPa (Figure 4.5b).

Figure 4.1 Pressure vs. density plot of Hugoniot data for MgSiO₃ glass and crystal from this study shown with previous Hugoniot data for porous material. Also shown is the excellent agreement between 298 K diamond anvil cell (DAC) data and 298 K isotherm of *Fiquet et al.* [2000]. The perovskite datum, also from *Fiquet et al.* [2000], at 67 GPa, 4.77 g/cm³ and 2900 K is more dense than Hugoniot data at same pressure, and temperature ~1500 K, indicating a lower density phase than perovskite along the Hugoniot in the 70 to 105 GPa range. Mixed phase regions apply to crystal Hugoniot only, as described in the text. Note increase in density along crystal Hugoniot observed at ~170 GPa and ~4500 K compared to decrease in density upon melting of an ultraporous mixture of MgO and fused SiO₂ shocked to perovskite at 30 GPa with a calculated temperature and density of 4000 K and 4.2 g/cm³. Standard errors calculated after *Jackson and Ahrens* [1979] are shown.

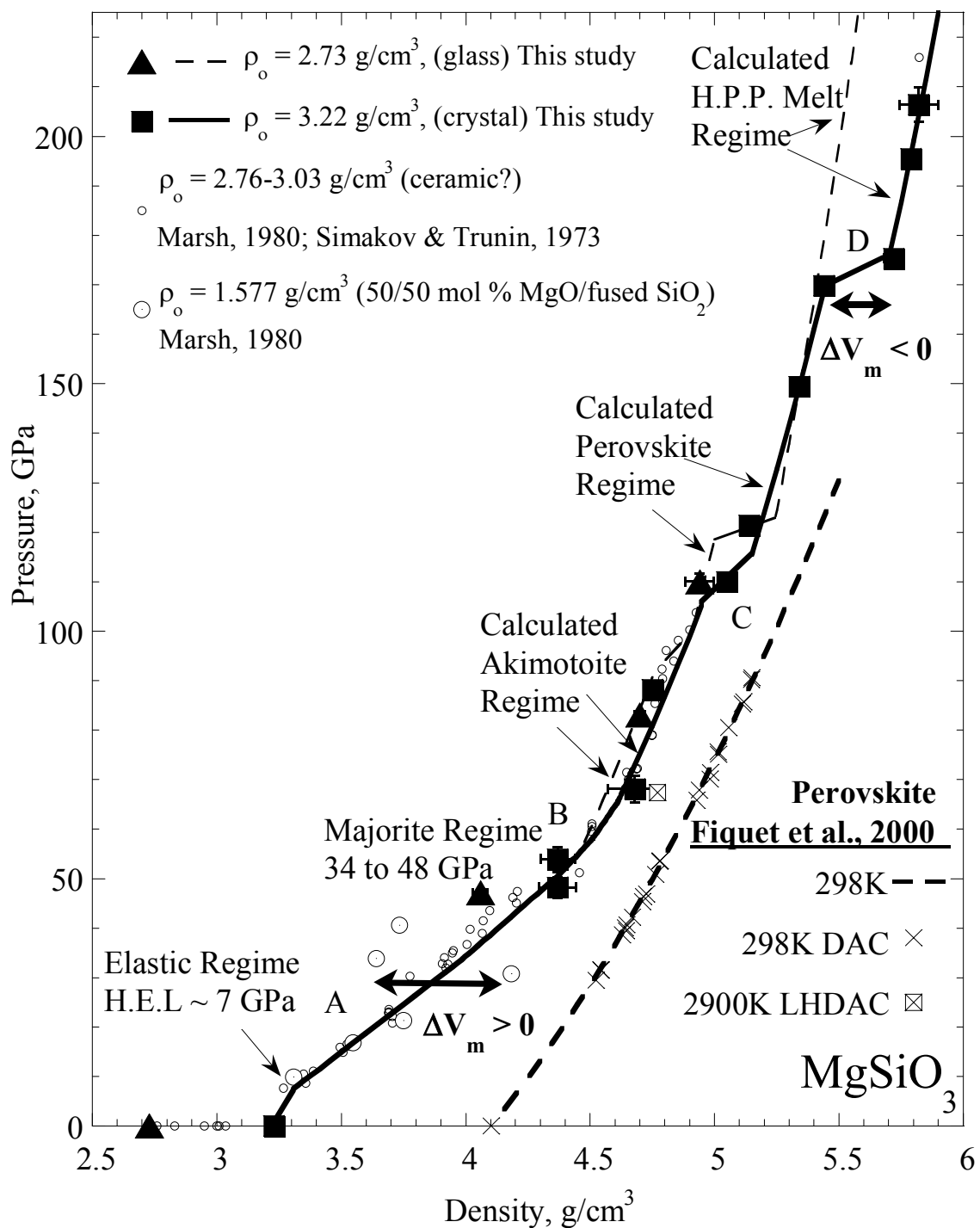


Figure 4.2 Calculated H.P.P. Hugoniot of enstatite, for the 10 – 100 GPa range. The data in the 70 – 105 GPa range are less dense than predicted for the perovskite structure. Based on calculated Hugoniot for candidate phases akimotoite is the phase most likely achieved along this segment. Crystal data < 70 GPa show evidence of two arrivals indicating a mixed phase regime as outlined in Figure 4.1. Overturned Hugoniot calculated for MgO/fused silica mix shocked to perovskite due to large thermal pressure. Decrease in density upon melting is in excellent agreement with calculations.

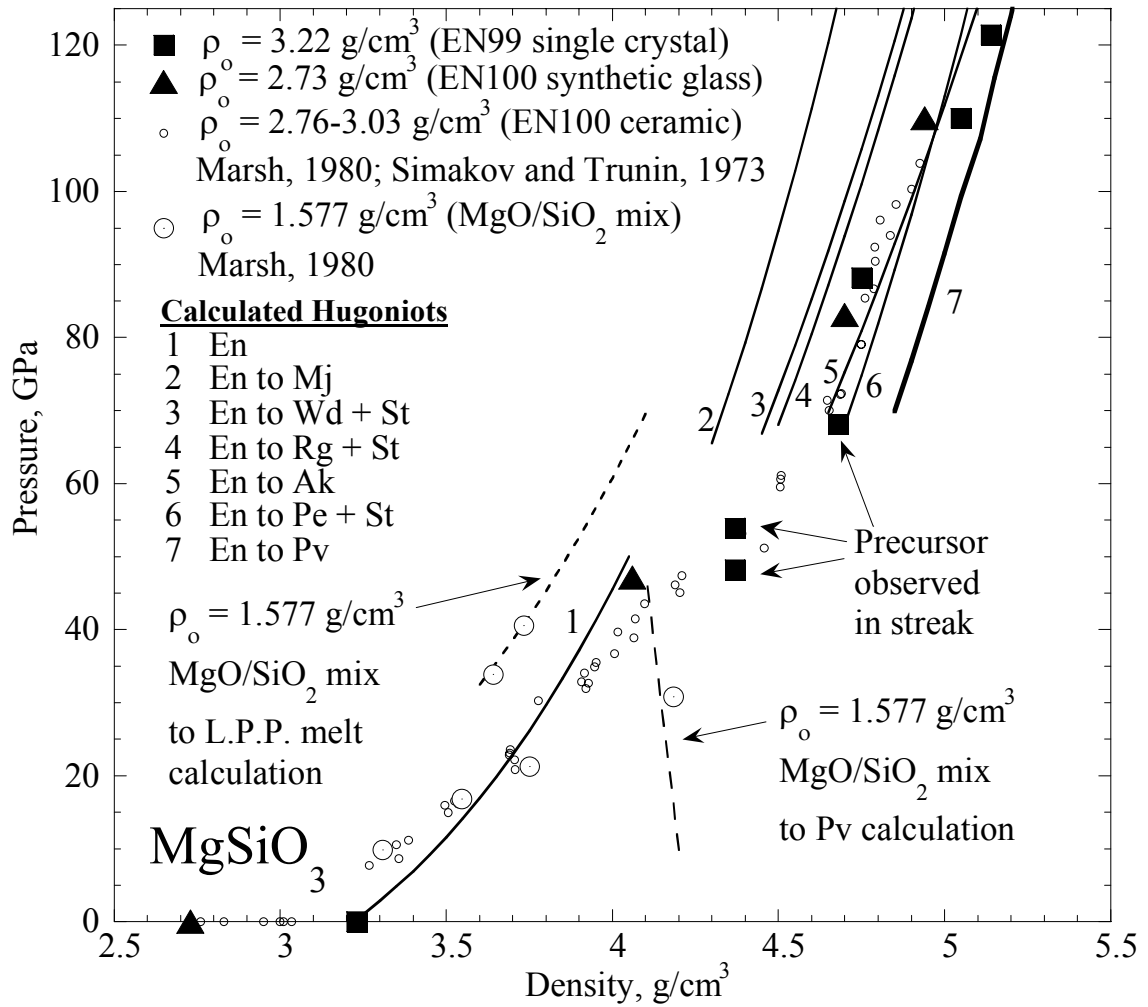


Figure 4.3 Calculated shock temperatures of candidate H.P.P. Hugoniot of enstatite for the 10 – 100 GPa range. Phases are all colder than their corresponding equilibrium phase regimes, except Rg + St. Calculated Hugoniot temperature of ultraporous mixture of MgO-SiO₂ shocked to perovskite and melt shown. Phase boundaries from *Presnall* [1995] except: Mj-Ak-Pv triple point [*Hirose et al.*, 2001]; Mj-melt-Pv triple point [*Ito and Katsura*, 1992]; and melting curve slope for $T > 2700$ K of [*Shen and Lazor*, 1995] (SL95), [*Sweeney and Heinz*, 1998] (SH98) and [*Boehler*, 2000] (B00). Clinoenstatite (CE). Orthoenstatite (OE). Protoenstatite field not shown.

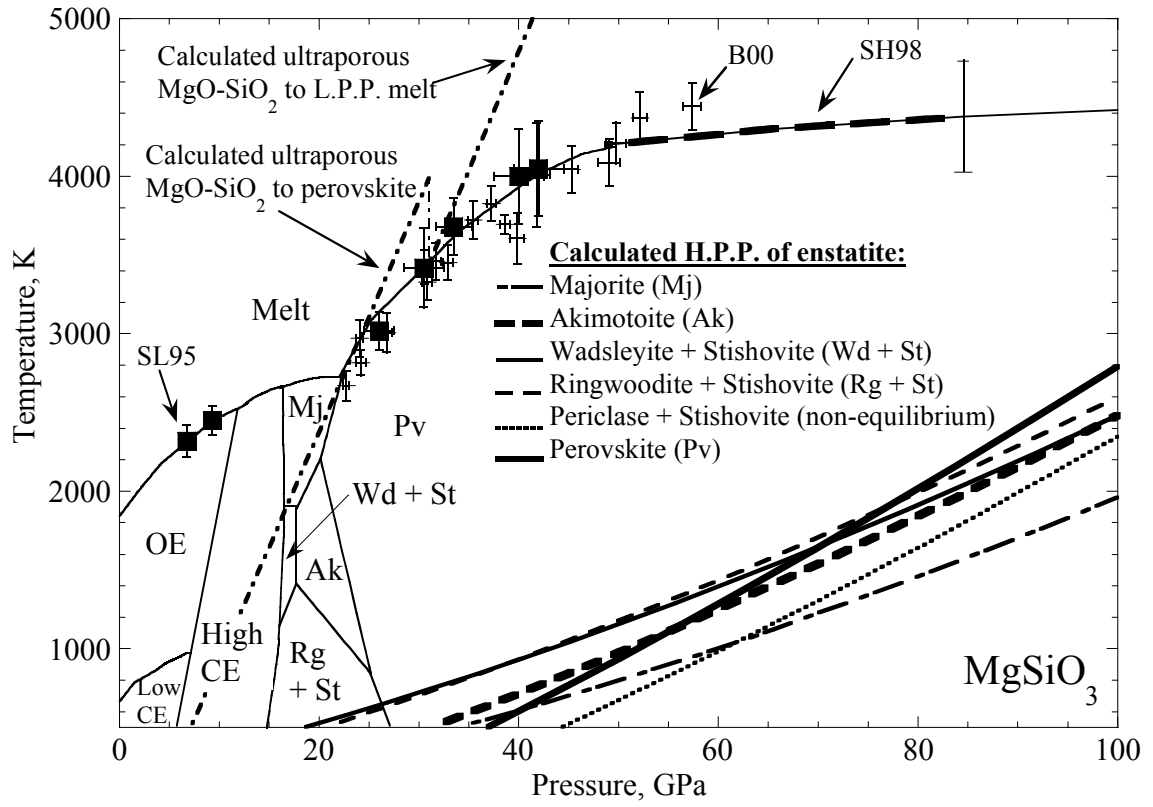


Figure 4.4 Calculated H.P.P. Hugoniots of enstatite indicate the perovskite structure is achieved in the 110 – 170 GPa range, followed by melting. Orientation of pre-shocked enstatite is shown for 3 shots. The presence of peak shock density for initial enstatite (001) on the perovskite and melt segments indicates the increase in density at ~170 GPa is not due to a denser Hugoniot achieved due to orientation, as observed in synthetic Mg_2SiO_4 [Furnish and Brown, 1986].

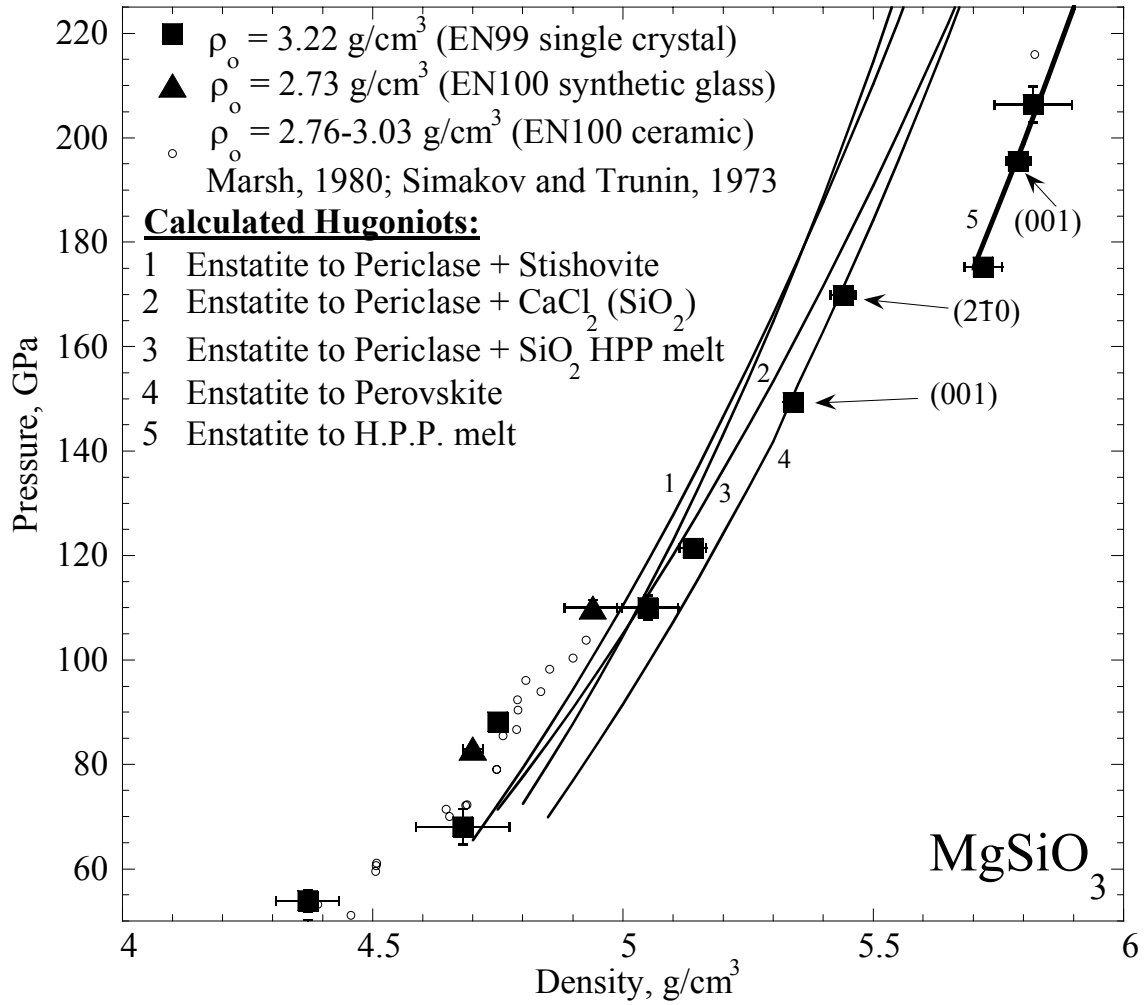
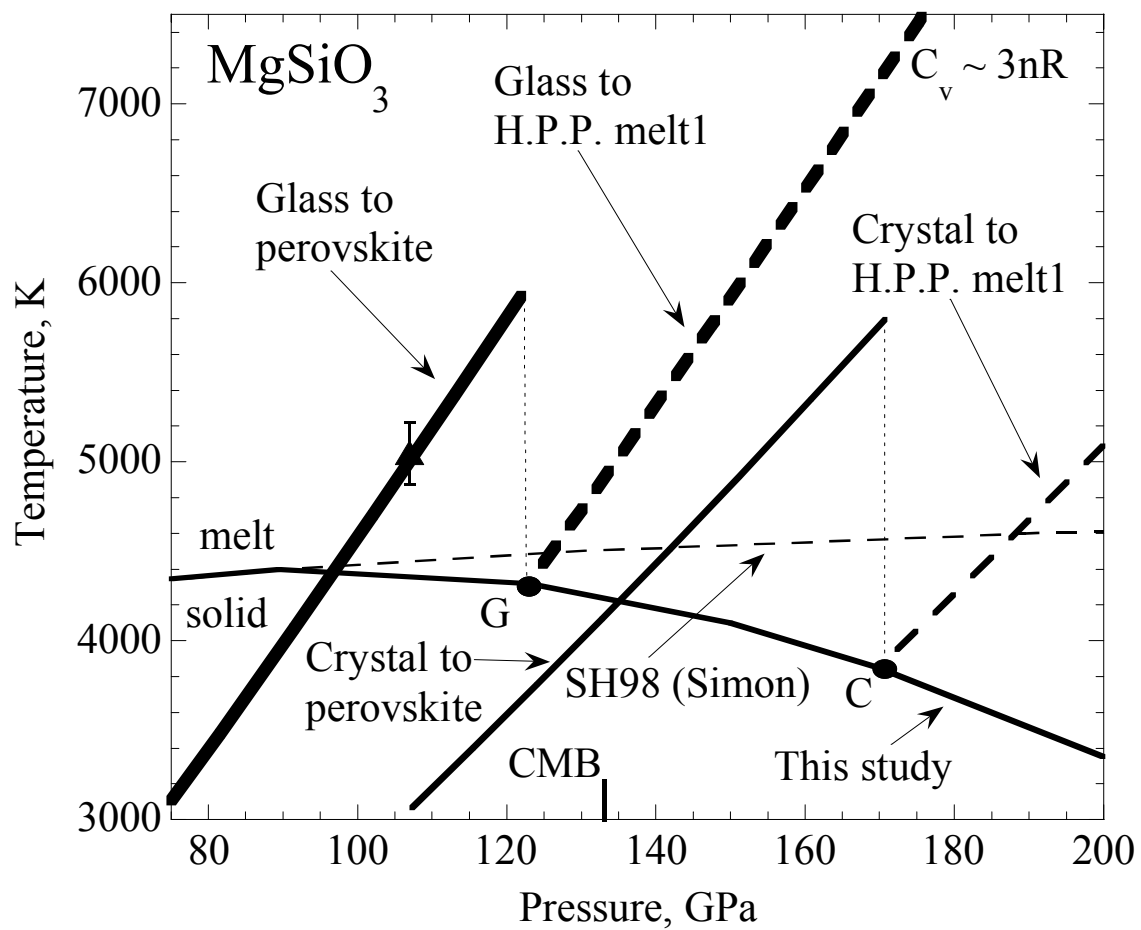


Figure 4.5 **a)** Temperature vs. pressure showing single measurement on MgSiO_3 synthetic glass at 107 ± 4 GPa and 5060 ± 173 K. Calculations of glass and enstatite shocked to final shock states of perovskite and H.P.P. melt1 are shown. Accounting for super-heating the melt transition of the crystal is fixed to ~ 170 GPa, as observed in the P- ρ data, and a melt Hugoniot temperature in agreement with a -10 K/GPa deviation, at 90 GPa, from the extrapolation of *Sweeney and Heinz* [1998] Simon melt equation, as constrained by their data up to 85 GPa. **b)** Calculations of glass and enstatite shocked to final shock states of perovskite and H.P.P. melt2 are shown assuming steeper melting curve of *Boehler* [2000] as shown in the figure up to 100 GPa compared to melting curve of part a).



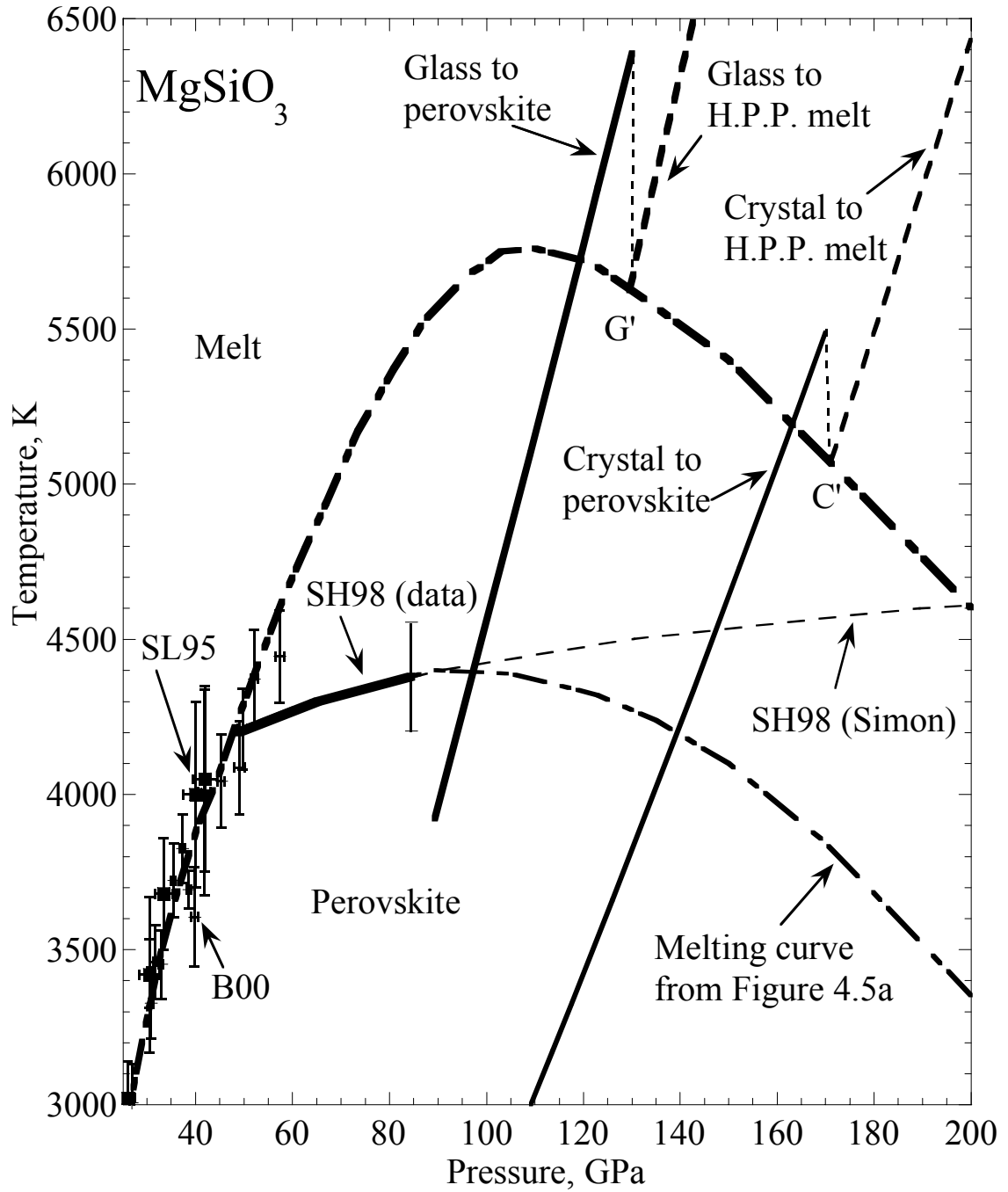


Figure 4.6 Change in volume upon melting, ΔV_m , (as a percentage of V_{solid}) constrained by the density jump along the crystal Hugoniot at 170 GPa as a function of thermal expansion of the solid (perovskite) for various temperature differences. ΔT used in calculation shown along each curve. Uncertainty in $\Delta V_m = 0$ shown by horizontal dashed lines. ΔV_m and α consistent with the three melting curves discussed in the text are shown: Simon (SH98) corresponds to extrapolation of *Sweeney and Heinz's* [1998] melting curve to 170 GPa; G-C corresponds to low temperature negative slope melting curve of Figure 4.5a; and G'-C' corresponds to high temperature more steeply sloped negative Clapeyron curve of Figure 4.5b. At 170 GPa it is unlikely the thermal expansivity of perovskite would be greater than $2.7 \times 10^{-5} \text{ K}^{-1}$, the value at 5000 K and room pressure.

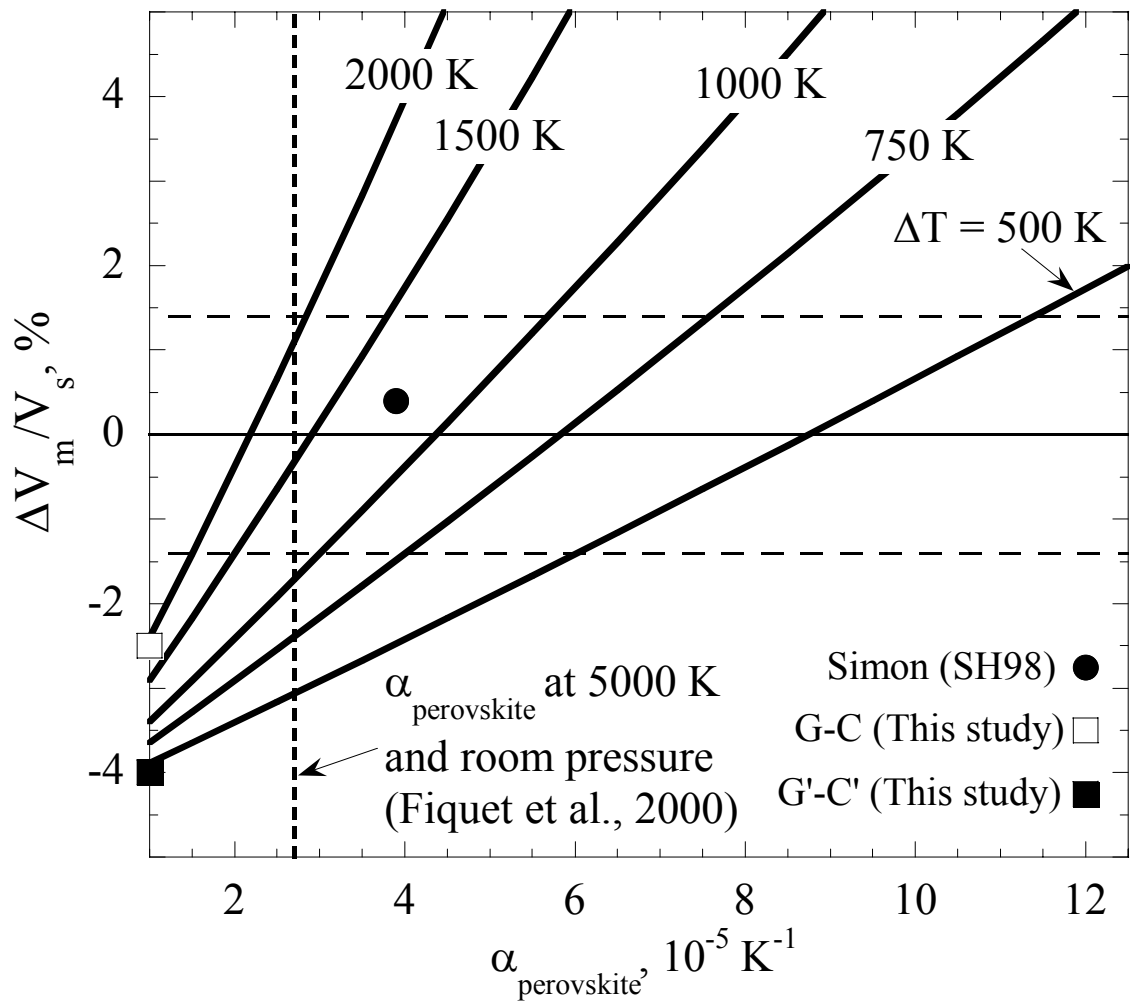
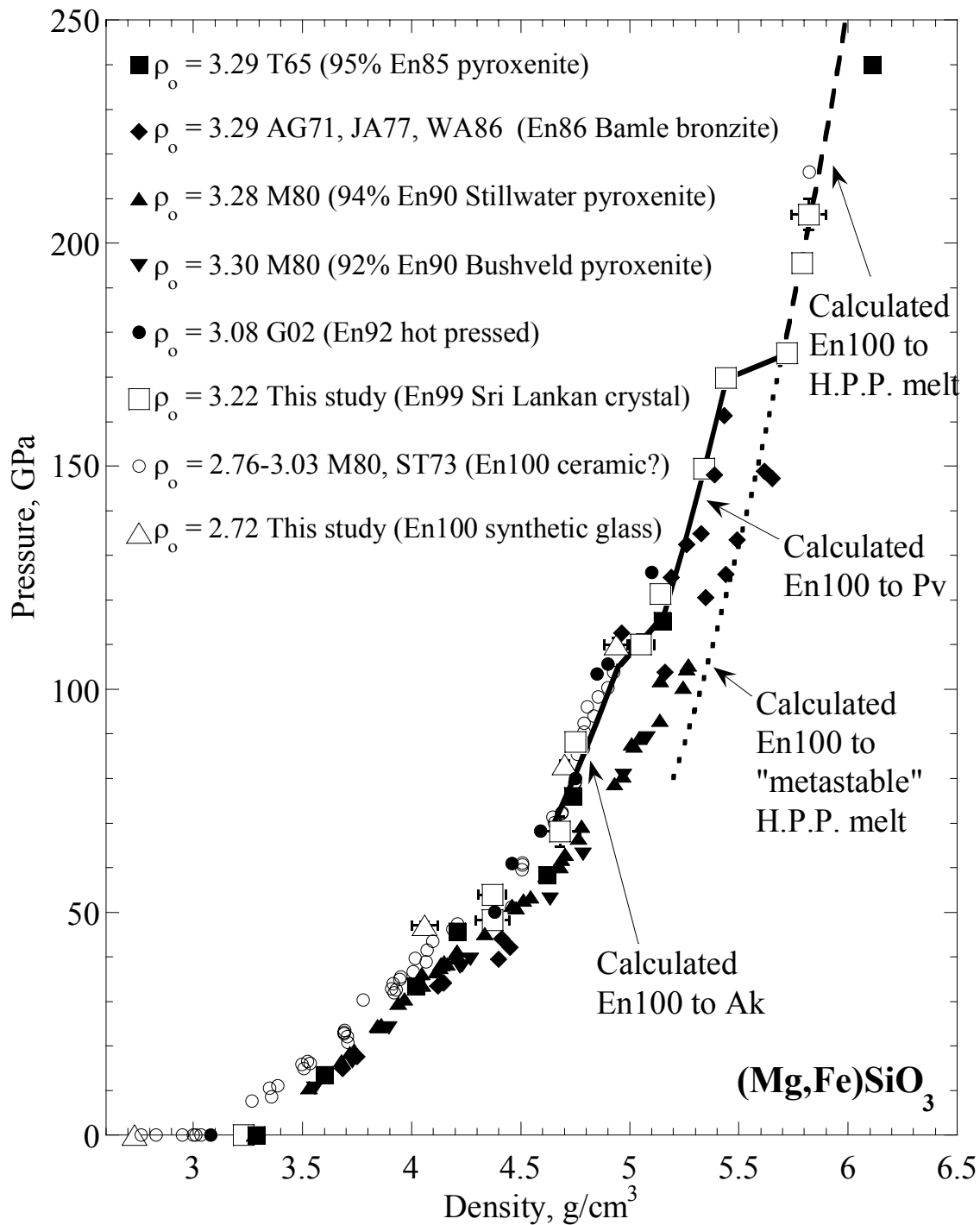


Figure 4.7 Pressure vs. density Hugoniot data for MgSiO_3 (open symbols) and $(\text{Mg}_{1-x}, \text{Fe}_x)\text{SiO}_3$, where $x = .08$ to $.15$ (closed symbols). En notation, i.e., En85 corresponds to $1-x$ in percent form. Bifurcation in $(\text{Mg,Fe})\text{SiO}_3$ data at 60 GPa shows Akimotoite and Perovskite phases achieved in similar pressure ranges as interpreted for MgSiO_3 data in Figure 4.2 with a higher density leg assumed to be due to lower compressibility. The low compressibility is most likely due to partial, or complete, melt occurring at lower pressures than expected due to impurities (pyroxenites), or alteration products (Bamle bronzite), not a phase transition to a more dense solid phase. [Trunin *et al.*, 1965] (T65); [Ahrens and Gaffney, 1971] (AG71); [Jeanloz and Ahrens, 1977] (JA77); [Watt and Ahrens, 1986] (WA86); [Marsh, 1980] (M80); [Gong *et al.*, 2001] (G02); [Simakov and Trunin, 1973] (ST73).



Bibliography

- Adadurov, G.A., A.N. Dremin, S.V. Pershin, V.N. Rodionov, and Y.N. Ryabinin, Shock compression of quartz (in Russian), *Prikl. Mekh. Fiz.*, 4, 81-89, 1962.
- Ahrens, T.J., Dynamic compression of earth materials, *Science*, 207, 1035-1041, 1980.
- Ahrens, T.J., Shock wave techniques for geophysics and planetary physics, in *Methods of Experimental Physics*, edited by C.G. Sammis, and T.L. Henyey, pp. 185-235, Academic Press, New York, 1987.
- Ahrens, T.J., and E.S. Gaffney, Dynamic compression of enstatite, *J. Geophys. Res.*, 76, 5504-5513, 1971.
- Ahrens, T.J., G.A. Lyzenga, and A.C. Mitchell, Temperatures induced by shock waves in minerals, in *High Pressure Research in Geophysics*, edited by S. Akimoto, and M.H. Manghnani, pp. 579-594, Cent. Acad. Pubs., Japan, 1982.
- Akins, J.A., and T.J. Ahrens, Dynamic compression of SiO₂: A new interpretation, *Geophys. Res. Lett.*, 29 (10), doi: 10.1029/2002GL014806, 2002.
- Anderson, O.L., *Equations of State of Solids for Geophysics and Ceramic Sciences*, 405 pp., Oxford Univ. Press, New York, 1995.
- Andrault, D., R.J. Angel, J. Mosenfelder, and T. Le Bihan, Equation of state of stishovite to lower mantle pressures, *Am. Mineral.*, 88, 301-307, 2003.
- Bass, J.D., Elasticity of minerals, glasses and melts, in *Mineral Physics and Crystallography: A Handbook of Physical Constants*, edited by T.J. Ahrens, pp. 45-63, American Geophysical Union, Washington, D.C., 1995.
- Bina, C.R., Lower mantle mineralogy and the geophysical perspective, in *Ultrahigh-pressure mineralogy: Physics and chemistry of the Earth's deep interior*, edited by R.J. Hemley, pp. 205-240, Miner. Soc. of Am., Washington, D.C., 1998.
- Boehler, R., High-pressure experiments and the phase diagram of lower mantle and core materials, *Rev. Geophys.*, 38, 221-245, 2000.
- Borshchevskii, A.O., M.M. Gorshkov, and A.M. Tarasov, The two-stage shock compression of quartzite to pressures of 550 - 1500 kbar (in Russian), *Izv. Earth Phys. (Engl. Transl.)*, 34, 291-294, 1998.

- Boslough, M., Postshock temperatures in silica, *J. Geophys. Res.*, *93*, 6477-6484, 1988.
- Brannon, P.T., C. Konrad, R.W. Morris, E.D. Jones, and J.R. Asay, Studies of the spectral and spatial characteristics of shock-induced luminescence from x-cut quartz, *J. Appl. Physics*, *54* (11), 6374-6381, 1983.
- Chao, E.C.T., J.J. Fahey, J. Littler, and D.J. Milton, Stishovite, SiO₂, a very high pressure new mineral from Meteor Crater, Arizona, *J. Geophys. Res.*, *67*, 419-421, 1962.
- Chen, M., T.G. Sharp, A. El Goresy, B. Wopenka, and X. Xie, The majorite-pyrope + magnesiowustite assemblage: Constraints on the history of shock veins in chondrites, *Science*, *271*, 1570-1573, 1996.
- Chhabildas, L.C., and J.M. Miller, Release-adiabat measurements in crystalline quartz, Report # SAND 85-1092, Sandia National Laboratory, Albuquerque, N.M., Albuquerque, NM, 1985.
- Cohen, R.E., Bonding and elasticity of stishovite SiO₂ at high pressure-linear augmented plane wave calculations, *Am. Mineral.*, *76*, 733-742, 1991.
- DeCarli, P.S., and D.J. Milton, Stishovite: Synthesis by shock wave, *Science*, *147*, 144-145, 1965.
- Dubrovinskaia, N.A., L.S. Dubrovinsky, S.K. Saxena, F. Tutti, S. Rekhi, and T. Le Bihan, Direct transition from cristobalite to post-stishovite alpha-PbO₂-like silica phase, *Euro. J. Mineral.*, *13*, 479-483, 2001.
- Dubrovinsky, L.S., N.A. Dubrovinskaia, S.K. Saxena, F. Tutti, S. Rekhi, T. Le Bihan, G.Y. Shen, and J. Hu, Pressure-induced transformations of cristobalite, *Chem. Phys. Lett.*, *333*, 264-270, 2001.
- Dubrovinsky, L.S., S.K. Saxena, P. Lazor, R. Ahuja, O. Eriksson, J.M. Willis, and B. Johansson, Experimental and theoretical identification of a new high-pressure phase of silica, *Nature*, *388*, 362-365, 1997.
- Duffy, T.S., Elastic properties of metals and minerals under shock compression, Ph.D. thesis, California Institute of Technology, Pasadena, CA, 1992.
- Duffy, T.S., and T.J. Ahrens, Sound velocities at high pressure and temperature and their geophysical implications, *J. Geophys. Res.*, *97*, 4503-4520, 1992.

- El Goresy, A., L. Dubrovinsky, T.G. Sharp, S.K. Saxena, and M. Chen, A monoclinic post-stishovite polymorph of silica in the Shergotty Meteorite, *Science*, 288, 1632-1634, 2000.
- Fiquet, G., A. Dewaele, D. Andrault, M. Kunz, and T. Le Bihan, Thermoelastic properties and crystal structure of MgSiO₃ perovskite at lower mantle pressure and temperature conditions, *Geophys. Res. Lett.*, 27 (1), 21-24, 2000.
- Fowles, R., Dynamic compression of quartz, *J. Geophys. Res.*, 72, 5729-5742, 1967.
- Furnish, M.D., and J.M. Brown, Shock loading of single crystal olivine in the 100-200 GPa range, *J. Geophys. Res.*, 91, 4723-4729, 1986.
- Gaines, R.V., H.C.W. Skinner, E.E. Foord, B. Mason, and A. Rosenzweig, *Dana's New Mineralogy*, 1820 pp., John Wiley & Sons, New York, NY, 1997.
- Gaminizoysa, E., Colourless enstatite from Embilipitiya, Sri Lanka, *Journal of Gemmology*, XIX (5), 419-425, 1985.
- Garnero, E.J., and D.V. Helmberger, A very slow basal layer underlying large-scale low-velocity anomalies in the lower mantle beneath the Pacific: Evidence from core phases, *Phys. Earth Planet. Inter.*, 91, 161-176, 1995.
- German, V.N., N.N. Orlova, L.A. Tarasova, and R.F. Trunin, Synthesis of the orthorhombic phase of silica in dynamic compression (in Russian), *Izv. Earth Phys. (Engl. Transl.)*, 7, 50-56, 1974.
- Gong, Z.Z., X. Li, and F. Jing, The possible composition and thermal structure of the earth's lower mantle and core, in *Shock compression of condensed matter - 2001*, edited by M.D. Furnish, N.N. Thadhani, and Y. Horie, pp. 1401-1405, American Institute of Physics, Atlanta, Georgia, 2001.
- Grady, D.E., W.I. Murri, and P.S. DeCarli, Hugoniot sound velocities and phase transformation in two silicates, *J. Geophys. Res.*, 80, 4857-4861, 1975.
- Grover, R., Liquid metal equation of state based on scaling, *J. Chem. Phys.*, 55, 3435-3441, 1971.
- Gwanmesia, G.D., J. Liu, G. Chen, S. Kesson, S.M. Rigden, and R.C. Liebermann, Elasticity of the pyrope (Mg₃Al₂Si₃O₁₂)-majorite (MgSiO₃) garnets solid solution, *Phys. Chem. Miner.*, 27, 445-452, 2000.

- Harding, R.R., E.A. Jobbins, B.R. Young, and C.H. Winter, Near-colourless Enstatite from Sri Lanka, *Journal of Gemmology*, XVIII (3), 213-216, 1982.
- Hirose, K., T. Komabayashi, and M. Murakami, In situ measurements of the majorite-akimotoite-perovskite phase transition boundaries in MgSiO₃, *Geophys. Res. Lett.*, 22 (23), 4351-4354, 2001.
- Ito, E., and T. Katsura, Melting of ferromagnesian silicates under lower mantle conditions, in *High Pressure Research: Application to Earth and Planetary Sciences*, edited by Y. Syono, and M. Manghnani, pp. 315-322, American Geophysical Union, Washington, D.C., 1992.
- Jackson, I., and T.J. Ahrens, Shock-wave compression of single crystal forsterite, *J. Geophys. Res.*, 84, 3039-3048, 1979.
- Jackson, I., and H. Niesler, The elasticity of periclase to 3 GPa and some geophysical implications, in *High Pressure Research in Geophysics*, edited by S. Akimoto, and M. Manghnani, pp. 93-133, Cen. Acad. Publ., Tokyo, Japan, 1982.
- Jackson, J.M., S.V. Sinogeikin, and J.D. Bass, Sound velocities and elastic properties of gamma -Mg₂SiO₄ to 873 K by Brillouin spectroscopy, *Am. Mineral.*, 85 (2), 296-303, 2000.
- Jakubith, M., and U. Hornemann, Majorite formation from enstatite by experimental shock-loading, *Phys. Earth Planet. Int.*, 27, 95-99, 1981.
- Jeanloz, R., and T.J. Ahrens, Pyroxenes and olivines: Structural implications of shock-wave data for high pressure phases, in *High-Pressure Research: Applications to Geophysics*, edited by M.H. Manghnani, and S. Akimoto, pp. 439-462, Academic, San Diego, Calif., 1977.
- Jeanloz, R., and T.J. Ahrens, Equations of state of FeO and CaO, *Geophys. J. R. Astr. Soc.*, 62, 505-528, 1980.
- Karki, B.B., L. Stixrude, and J. Crain, Ab initio elasticity of three high-pressure polymorphs of silica, *Geophys. Res. Lett.*, 24, 3269-3272, 1997.
- Karki, B.B., L. Stixrude, and R.M. Wentzcovitch, High-pressure elastic properties of major materials of Earth's mantle from first principles, *Rev. Geophys.*, 39 (4), 507-534, 2001.
- Kiefer, B., L. Stixrude, and R.M. Wentzcovitch, Calculated elastic constants and anisotropy of Mg₂SiO₄ spinel at high pressure, *Geophys. Res. Lett.*, 24 (22), 2841-2844, 1997.

- Kingma, K.J., R.E. Cohen, R.J. Hemley, and H.-K. Mao, Transformation of stishovite to a denser phase at lower-mantle pressures, *Nature*, 374, 243-245, 1995.
- Lange, R.A., and I.S.E. Carmichael, Densities of Na₂O-K₂O-CaO-MgO-FeO-Fe₂O₃-Al₂O₃-TiO₂-SiO₂ liquids: New measurements and derived partial molar properties, *Geochim. Cosmochim. Acta*, 51, 2931-2946, 1987.
- Li, B.S., and R.C. Liebermann, Sound velocities of wadsleyite β -(Mg_{0.88},Fe_{0.12})SiO₄ to 10 GPa, *Am. Mineral.*, 85 (2), 292-295, 2000.
- Luo, S., T. Çağın, A. Strachan, W.A. Goddard III, and T.J. Ahrens, Molecular dynamics modeling of stishovite, *Earth Planet. Sci. Lett.*, 202, 147-157, 2002a.
- Luo, S., J.L. Mosenfelder, P.D. Asimow, and T.J. Ahrens, Direct shock wave loading of stishovite to 235 GPa: Implications for perovskite stability relative to oxide assemblage at lower mantle conditions, *Geophys. Res. Lett.*, 29, 10.1029/2002GL015627, 36-1 to 36-4, 2002b.
- Lyzenga, G.A., Shock temperatures of materials: Experiments and application to the high pressure equation of state, Ph.D. thesis, California Institute of Technology, Pasadena, CA, 1980.
- Lyzenga, G.A., T.J. Ahrens, and A.C. Mitchell, Shock temperatures of SiO₂ and their geophysical implications, *J. Geophys. Res.*, 88, 2431-2444, 1983.
- Marsh, S.P., *LASL Shock Hugoniot Data*, 658 pp., University of California Press, Berkeley, 1980.
- Marton, F.C., J. Ita, and R.E. Cohen, P-V-T equation of state of MgSiO₃ perovskite from molecular dynamics and constraints on lower mantle composition, *J. Geophys. Res.*, 106, 8615-8627, 2001.
- McQueen, R.G., The velocity of sound behind strong shocks in SiO₂, in *Shock Compression of Condensed Matter 1991*, edited by S.C. Schmidt, R.D. Dick, J.W. Forbes, and D.G. Tasker, pp. 75-78, Elsevier, 1991.
- McQueen, R.G., and J.N. Fritz, Some techniques and results from high-pressure shock-wave experiments utilizing the radiation from shocked transparent materials, in *Shock Wave in Condensed Matter - 1981*, edited by W.J. Nellis, L. Seaman, and R.A. Graham, pp. 193-207, Am. Inst. Phys., New York, 1982.
- McQueen, R.G., J.N. Fritz, and S.P. Marsh, On the equation of state of stishovite, *J. Geophys. Res.*, 68, 2319-2322, 1963.

- McQueen, R.G., S.P. Marsh, and J.N. Fritz, Hugoniot equation of state of twelve rocks, *J. Geophys. Res.*, 72, 4999-5036, 1967.
- Meade, C., H.K. Mao, and J.Z. Hu, High-temperature phase-transition and dissociation of (Mg,Fe)SiO₃ perovskite at lower mantle pressures, *Science*, 268, 1743-1745, 1995.
- Mitchell, A.C., and W.J. Nellis, Shock compression of aluminum, copper, and tantalum, *J. Appl. Phys.*, 52 (5), 3363-3374, 1981.
- Morgan, V.J., and J.N. Fritz, Sound velocity and SiO₂ Hugoniots, in *High Pressure Science and Technology*, edited by K.D. Timmerhaus, and M.S. Barger, pp. 109-115, Plenum Publishing Corp., New York, 1979.
- Morimoto, N., J. Fabries, A.K. Ferguson, I.V. Ginzburg, M. Ross, F.A. Siefert, J. Zussman, K. Aoki, and G. Gottardi, Nomenclature of pyroxenes, *Am. Mineral.*, 73, 1123-1133, 1988.
- Murakami, M., K. Hirose, S. Ono, and Y. Ohishi, Stability of CaCl₂-type and alpha-PbO₂ type SiO₂ at high pressure and temperature determined by in-situ X-ray measurements, *Geophys. Res. Lett.*, 30 (5), art. no. 1207, 2003.
- Navrotsky, A., Thermodynamic properties of minerals, in *Mineral Physics and Crystallography: A Handbook of Physical Constants*, edited by T.J. Ahrens, pp. 18-28, American Geophysical Union, Washington DC, 1995.
- Oganov, A.R., G.D. Price, and M.J. Gillan, Structural stability of silica at high pressures and temperatures, In prep., 2003.
- Ono, S., K. Hirose, M. Murakami, and M. Isshiki, Post-stishovite phase boundary in SiO₂ determined by in situ X-ray observations, *Earth Planet. Sci. Lett.*, 197, 187-192, 2002.
- Panero, W.R., L.R. Benedetti, and R. Jeanloz, Equation of state of stishovite and interpretation of SiO₂ shock compression data, *J. Geophys. Res.*, 108 (B1), 5-1 - 5-7, 2003.
- Piekarz, P., P.T. Jochym, K. Parlinski, and J. Lazewski, High-pressure and thermal properties of gamma-Mg₂SiO₄ from first-principles calculations, *J. Chem. Phys.*, 117 (7), 3340-3344, 2002.
- Podurets, M.A., L.V. Popov, A.G. Sevast'yanova, G.V. Simakov, and R.F. Trunin, On the relation between the size of studied specimens and the position of the silica shock adiabat (in Russian), *Izv. Phys. Solid Earth (Engl. Transl.)*, 11, 727-728, 1976.

- Podurets, M.A., G.V. Simakov, G.S. Telegin, and R.F. Trunin, Polymorphism of silica in shock waves and equation of state of coesite and stishovite (in Russian), *Izv. Earth Phys. (Engl. Transl.)*, 17, 9-15, 1981.
- Podurets, M.A., G.V. Simakov, and R.F. Trunin, Stishovite transition to a denser phase (in Russian), *Izv. Earth Phys. (Engl. Transl.)*, 26, 295-300, 1990.
- Presnall, D.C., Phase diagrams of Earth-forming minerals, in *Minerals Physics and Crystallography: A Handbook of Physical Constants*, edited by T.J. Ahrens, pp. 248-268, Amer. Geophys. U., Washington DC, 1995.
- Reynard, B., and D.C. Rubie, High-pressure, high temperature Raman spectroscopic study of ilmenite-type MgSiO_3 , *Am. Mineral.*, 81 (9-10), 1092-1096, 1996.
- Rigden, S.M., T.J. Ahrens, and E.M. Stolper, High-pressure equation of state of molten anorthite and diopside, *J. Geophys. Res.*, 94, 9508-9522, 1989.
- Ringwood, A.E., *Composition and Petrology of the Earth's Mantle*, 618 pp., McGraw-Hill, New York, 1975.
- Saxena, S.K., L.S. Dubrovinsky, P. Lazor, Y. Cerenius, P. Haggkvist, M. Hanfland, and J.Z. Hu, Stability of perovskite (MgSiO_3) in the Earth's mantle, *Science*, 274, 1357-1359, 1996.
- Schmitt, D.R., B. Svendsen, and T.J. Ahrens, Shock-induced radiation from minerals, in *Shock Waves in Condensed Matter*, edited by Y.M. Gupta, pp. 261-265, Plenum Press, New York, 1986.
- Serghiou, G., A. Zerr, and R. Boehler, $(\text{Mg,Fe})\text{SiO}_3$ -perovskite stability under lower mantle conditions, *Science*, 280, 2093-2095, 1998.
- Sharp, T.G., C.M. Lingemann, C. Dupas, and D. Stöfler, Natural occurrence of MgSiO_3 -ilmenite and evidence for MgSiO_3 -perovskite in a shocked L chondrite, *Science*, 277, 352-355, 1997.
- Shen, G.Y., and P. Lazor, Measurement of melting temperatures of some minerals under lower mantle pressures, *J. Geophys. Res.*, 100, 17699-17713, 1995.
- Shieh, S.R., T.S. Duffy, and B. Li, Strength and elasticity of SiO_2 across the stishovite- CaCl_2 structural phase boundary, *Phys. Rev. Lett.*, 89 (25), 2555071-3, 2002.
- Shim, S.H., T.S. Duffy, and G.Y. Shen, Stability and structure of MgSiO_3 perovskite to 2300-kilometer depth in Earth's mantle, *Science*, 293, 2437-2440, 2001.

- Simakov, G.V., and R.F. Trunin, On the existence of the overdense perovskite structures in magnesian silicates under conditions of high pressure (in Russian), *Izv. Earth Phys. (Engl. Transl.)*, *9*, 603-604, 1973.
- Smith, J.V., and B. Mason, Pyroxene-garnet transformation in Coorara Meteorite, *Science*, *168*, 832-833, 1970.
- Speziale, S., C.S. Zha, T.S. Duffy, R.J. Hemley, and H.K. Mao, Quasi-hydrostatic compression of magnesium oxide to 52 GPA: Implications for the P-V-T equation of state, *J. Geophys. Res.*, *106*, 515-528, 2001.
- Stishov, S.M., and S.V. Popova, New dense polymorphic modification of silica (in Russian), *Geokh.*, *10*, 837-839, 1961.
- Stixrude, L., and M.S.T. Bukowinski, Thermodynamic analysis of the system MgO-FeO-SiO₂ at high pressure and the structure of the lowermost mantle, in *Evolution of the Earth and Planets, Geophysical Monograph*, pp. 131-141, IUGG, 1993.
- Stöffler, D., Minerals in the deep Earth: A message from the asteroid belt, *Science*, *278*, 1576-1577, 1997.
- Sugiura, H., K. Kondo, and A. Sawaoka, Shock temperatures in fused silica measured by optical technique, *J. Appl. Phys.*, *53*, 4512-4514, 1982.
- Svensden, B., and T.J. Ahrens, Shock-induced temperatures of MgO, *Geophys. J. R. Astr. Soc.*, *91*, 667-691, 1987.
- Sweeney, J.S., and D.L. Heinz, Laser-heating through a diamond-anvil cell: Melting at high pressures, in *Properties of Earth and Planetary Materials at High Pressure and Temperature*, edited by M. Manghnani, and T. Yagi, pp. 197-213, A. G. U., Washington, D.C., 1998.
- Teter, D.M., R.J. Hemley, G. Kresse, and J. Hafner, High pressure polymorphism in silica, *Phys. Rev. Lett.*, *80*, 2145-2148, 1998.
- Tomioka, N., K. Fujino, E. Ito, T. Katsura, T. Sharp, and T. Kato, Microstructures and structural phase transition in (Mg,Fe)SiO₃ majorite, *Eur. J. Mineral.*, *14*, 7-14, 2002.
- Trunin, R.F., V.I. Gon'shakova, G.V. Simakov, and N.E. Galdin, A study of rocks under the high pressures and temperatures created by shock compression (in Russian), *Izv. Earth Phys. (Engl. Transl.)*, *9*, 579-586, 1965.

- Trunin, R.F., G.V. Simakov, M.A. Podurets, B.N. Moiseyev, and L.V. Popov, Dynamic compressibility of quartz and quartzite at high pressure (in Russian), *Izv. Phys. Solid Earth (Engl. Transl.)*, 1, 8-12, 1971.
- Tsuchida, Y., and T. Yagi, A new post-stishovite high-pressure polymorph of silica, *Nature*, 340, 217-220, 1989.
- Wackerle, J., Shock-wave compression of quartz, *J. Appl. Phys.*, 33, 922-937, 1962.
- Watt, J.P., and T.J. Ahrens, Shock-wave equation of state of enstatite, *J. Geophys. Res.*, 91, 7495-7503, 1986.
- Watt, J.P., G.G. Davies, and R.J. O'Connell, The elastic properties of composite materials, *Rev. Geophys. Space Phys.*, 14, 541-563, 1976.
- Webb, S.L., and I. Jackson, The pressure dependence of the elastic moduli of single-crystal orthopyroxene ($\text{Mg}_{0.8}\text{Fe}_{0.2}\text{SiO}_3$), *Eur. J. Mineral.*, 5, 1111-1119, 1993.
- Weidner, D.J., J.D. Bass, A.E. Ringwood, and W. Sinclair, The single-crystal elastic moduli of stishovite, *J. Geophys. Res.*, 87, 4740-4746, 1982.
- Weidner, D.J., and E. Ito, Elasticity of MgSiO_3 in the ilmenite phase, *Phys. Earth Planet. Int.*, 40, 65-70, 1985.
- Weidner, D.J., H. Wang, and J. Ito, Elasticity of orthoenstatite, *Phys. Earth Planet. Int.*, 17 (2), 7-13, 1978.
- Williams, Q., and E.J. Garnero, Seismic evidence for partial melt at the base of Earth's mantle, *Science*, 273, 1528-1530, 1996.
- Yang, H.X., and S. Ghose, In-situ Fe-Mg order-disorder studies and thermodynamic properties of orthopyroxene ($\text{Mg,Fe})_2\text{Si}_2\text{O}_6$, *Am. Mineral.*, 79 (7-8), 633-643, 1994.
- Yang, W., Impact volatilization of calcite and anhydrite and the effects on global climate from the K/T impact crater at Chicxulub, Ph. D. thesis, California Institute of Technology, Pasadena, CA, 1996.
- Yeganeh-Haeri, A., Synthesis and re-investigation of the elastic properties of single crystal magnesium silicate perovskite, *Phys. Earth Planet. Int.*, 87, 111-121, 1994.
- Zhugin, Y.N., K.K. Krupnikov, N.P. Voloshin, and Y.A. Shoidin, Phase transformations in quartz, induced by shock waves from underground nuclear explosions (in Russian), *Izv. Phys. Solid Earth (Engl. Transl.)*, 35, 478-483, 1999.